Geosci. Model Dev., 17, 1765–1787, 2024
https://doi.org/10.5194/gmd-17-1765-2024

Geoscientific Model Development
Open Access
EGU

Towards variance-conserving reconstructions of climate indices with Gaussian process regression in an embedding space

Marlene Klockmann[1,a], **Udo von Toussaint**[2], **and Eduardo Zorita**[1]

[1]Institute for Coastal Systems – Analysis and Modelling, Helmholtz-Zentrum Hereon, Geesthacht, Germany
[2]Max Planck Institute for Plasma Physics, Garching, Germany
[a]now at: Institute of Oceanography, Universität Hamburg, Hamburg, Germany

Correspondence: Marlene Klockmann (marlene.klockmann@uni-hamburg.de)

Received: 4 February 2022 – Discussion started: 5 April 2022
Revised: 31 August 2023 – Accepted: 17 January 2024 – Published: 28 February 2024

Abstract. We present a new framework for the reconstruction of climate indices based on proxy data such as tree rings. The framework is based on the supervised learning method Gaussian Process Regression (GPR) and aims at preserving the amplitude of past climate variability. It can adequately handle noise-contaminated proxies and variable proxy availability over time. To this end, the GPR is formulated in a modified input space, termed here embedding space. We test the new framework for the reconstruction of the Atlantic multi-decadal variability (AMV) in a controlled environment with pseudo-proxies derived from coupled climate-model simulations. In this test environment, the GPR outperforms benchmark reconstructions based on multi-linear principal component regression. On AMV-relevant timescales, i.e. multi-decadal, the GPR is able to reconstruct the true amplitude of variability even if the proxies contain a realistic non-climatic noise signal and become sparser back in time. Thus, we conclude that the embedded GPR framework is a highly promising tool for climate-index reconstructions.

1 Introduction

Climate indices are important measures to describe the evolution of climate on regional, hemispheric or global scales in a condensed way. They reveal relevant timescales of climate variability and, in some cases, also subspaces that are important for predictability. Paramount examples are the El Niño–Southern Oscillation, the North Atlantic Oscillation and the Atlantic multi-decadal variability (AMV). To understand whether the typical timescales and magnitude of climate variability have been stationary over time or whether they have changed, e.g. with anthropogenic climate change, we need a long-term perspective on these climate indices. The index time series must not only cover the historical period of the past 150 years but also the period of interest, e.g. the past 1000–2000 years (Common Era). To obtain these long time series we need information from so-called climate proxies (e.g. tree rings and sediment cores) in combination with sophisticated statistical models to reconstruct the climate indices from the proxy data. We present a new machine learning framework for climate-index reconstructions and test its skill for reconstructing the AMV.

The AMV is an important index that describes the North Atlantic climate variability on decadal and longer timescales. Different definitions of the AMV have been developed over time, but the basic definition relies on the low-pass-filtered spatial average of sea surface temperature anomalies over the North Atlantic. Observations starting in about 1850 indicate that the AMV varies on typical timescales of 30–60 years. The state of the AMV plays a key role for many relevant climate phenomena such as Arctic sea-ice anomalies (Miles et al., 2014), North American and European summer climate, hurricane seasons and Sahel rainfall (Zhang and Delworth, 2006; Zhang et al., 2007). Both atmospheric as well as oceanic processes have been suggested as possible drivers of the AMV (e.g. Clement et al., 2015; Zhang et al., 2019; Yan et al., 2019; Garuba et al., 2018). It is not clear how much of the AMV is generated by internal climate variability and how much is generated by changes in external radiative forcing, i.e. volcanic and anthropogenic aerosols, solar insolation and

greenhouse gas concentrations (Haustein et al., 2019; Mann et al., 2021).

The observational period of approximately 150 years is not sufficient to provide a long-term perspective on the AMV or in fact any climate index that describes variability on multi-decadal and longer timescales. Therefore, longer time series are needed. These time series are typically derived from climate reconstructions based on climate proxies such as tree rings, bivalves or coral skeletons (e.g. Gray et al., 2004; Mann et al., 2008; Svendsen et al., 2014; Wang et al., 2017; Singh et al., 2018). This kind of reconstruction is based on statistical models that link the target index with proxy time series, using the observational period to calibrate their parameters. The trained models then use the much longer proxy time series as input to provide an estimation of the target index in the past.

Existing AMV reconstructions disagree on the amplitude and timing of AMV variability, especially prior to the beginning of the 18th century (Wang et al., 2017). As a consequence, they also provide conflicting views on the AMV response to external forcing (Knudsen et al., 2014; Wang et al., 2017; Zhang et al., 2019; Mann et al., 2022). Possible reasons for this disagreement are numerous. In general, the reconstructed variability will depend on the predictor data, i.e. the number, quality and locations of the proxies. Previous AMV reconstructions differed in their employed proxy networks and types, using only terrestrial or also marine records. As an example, including marine records seems to yield better reconstructions of AMV variability (e.g. Saenger et al., 2009; Mette et al., 2021). Proxy data are only available at a limited number of locations on the globe (see e.g. PAGES2k, 2017), and their availability decreases further back in time. Proxies also contain varying amounts of non-climatic signals, i.e. noise.

Existing reconstruction methods range from very simple linear methods such as composite plus scaling (Jones and Mann, 2004) or principal component analysis (e.g. Gray et al., 2004), over more complex linear methods such as Bayesian hierarchical modelling (Barboza et al., 2014) to non-linear methods such as random forest (Michel et al., 2020), pairwise comparison (Hanhijärvi et al., 2013) or data assimilation (e.g. Singh et al., 2018). The presence of noise or mutually unrelated variability may result in biased estimations of parameters of the statistical models such as regression coefficients. Especially regression-based methods are known to underestimate the true magnitude of variability, especially on lower frequencies (Zorita et al., 2003; Esper et al., 2005; Von Storch et al., 2004; Christiansen et al., 2009). They also tend to "regress to the mean", i.e. they have difficulties in reconstructing values that lie outside the range of the calibration data. This is further exacerbated by the presence of strong warming trends and shortness of the available calibration period (approximately 150 years).

Thus, robust reconstruction methods are needed in order to produce more reliable estimates of the amplitude of the past variability of the AMV in order to better quantify its response to external forcing. This is also a precondition for an unbiased detection of any "unusual" observed trends and for the subsequent attribution of those trends to a particular forcing, e.g. anthropogenic greenhouse gases. To this end, we need to design reconstruction methods which are more robust against noise and, importantly, do not strongly "regress to the mean" when the predictors become more noisy or scarce back in time. As in many disciplines, machine learning methods have successfully gained traction in the climate reconstruction community (e.g. Michel et al., 2020; Zhang et al., 2022; Wegmann and Jaume-Santero, 2023). Here, we explore the potential of the non-linear supervised learning method Gaussian process regression (GPR) for climate index reconstructions. GPR finds growing use in climate applications such as climate model emulators (Mansfield et al., 2020) or reconstructions of sea level fields (Kopp et al., 2016) and global mean surface temperature (Büntgen et al., 2021).

Unlike other machine learning methods, such as neural networks, GPR offers greater transparency and is less of a "black box". The number of free parameters is usually much smaller and ideally the parameters have a more direct physical interpretation. A Gaussian process (GP) describes a distribution over functions with a given mean and covariance structure. The covariance structure is chosen such that the resulting functions best match a given set of observations. This setup appears as more intuitive and closer to the more familiar family of regression methods than convoluted deep learning structures, which in the end may need additional algorithms for their physical interpretation. GPR's non-parametric nature has the advantage that we do not need to make any assumptions about the (non-)linearity of the underlying reconstruction problem. As a Bayesian method, GPR comes with its own uncertainty estimates, which is a very important feature for paleoclimate applications.

We do not only test GPR as a climate index reconstruction tool but also propose a modified input space for the GPR-based reconstructions. To this end, we embed the entire available dataset (proxy data and the target index) in a virtual space. The location of the data time series in this space are based on the similarity between the time series. The resulting cloud of data points in this virtual space can be viewed as a temporal sequence of images with missing values. The covariance of the GP describes the cross-correlation between the proxy records and the target index across time and virtual space. We use the GPR to fill the missing values where we do not have observations of the target index. This approach is somewhat similar to kriging in geostatistics, where two-dimensional fields are reconstructed based on point measurements and a known covariance structure. In our case, the input space is not the geographical space but the virtual embedding space and the covariance structure is learned from the data. This setup has the additional advantage that it can easily accommodate variable proxy availability in time and

that the proxy-related uncertainty can be directly accounted for by the parameters of the GP.

To fully judge the methodological performance and related uncertainties, reconstruction methods need to be tested in so-called pseudo-proxy experiments (Smerdon, 2012). Many methods have already been tested in such controlled environments, but the evaluation often lacks a thorough assessment of the method's capability to reconstruct the magnitude of the variability on different timescales. In particular, a reconstruction method must be able to capture extreme phases, again to ascertain whether the AMV is sensitive to sudden changes in the external forcing, e.g. after volcanic eruptions, but also to capture possible large internally generated variations, which could occur independent of external forcing. Here, we test our proposed framework of the embedded GPR in such a pseudo-proxy environment and place special emphasis on the method's skill of reconstructing extreme phases and the magnitude of variability of the AMV.

2 Methods and data

2.1 Pseudo-proxies and simulated AMV index

We generate the pseudo-proxies from a simulation of the Common Era (i.e. the past 2000 years) with the Max Planck Institute Earth System Model (MPI-ESM). The model version corresponds to the MPI-ESM-P LR setup used in the fifth phase of the Coupled Model Intercomparison Project (CMIP5, Giorgetta et al., 2013). A detailed description of the simulation can be found in Zhang et al. (2022). The target of the pseudo-reconstructions is the simulated AMV index (AMVI). We define the AMVI as the spatial mean of annually averaged sea surface temperature anomalies (SST) in the North Atlantic (0–70° N and 80° W to 0° E). The SST anomalies are calculated against the mean over the entire simulation period. We do not further detrend the AMVI because it is difficult to define a meaningful trend period in the paleocontext. In the case of real reconstructions, all proxies and the AMVI would be available for overlapping periods with different length, and it is not possible to define a meaningful common trend that could be subtracted from all records.

The pseudo-proxies are defined as time series of the simulated temperature at the model grid points closest to existing proxy sites in the PAGES2k database (PAGES2k, 2017). Over land, we use a 2 m annual mean air temperature and over ocean we use annual mean sea surface temperature. We do not use all available proxy sites from the PAGES2k database but only a subset thereof. We limit our selection of proxy sites to those within the North Atlantic domain (10–90° N and 100° W to 30° E) with annual resolution or finer. Out of these sites, we further select only those locations at which the pseudo-proxies have a correlation of 0.35 or higher with the AMVI during the last 150 simulation years. (In this case, both the AMVI and the pseudo-proxies are detrended before calculating the correlation.) The final proxy network consists of 23 pseudo-proxies (Fig. 1a).

We design three sets of pseudo-proxies to account for different sources of uncertainty: in the first test case (TCppp), we use perfect pseudo-proxies, i.e. the pseudo-proxies contain only the temperature signal. In the second test case (TCnpp), we use noisy pseudo-proxies, i.e. the pseudo-proxies contain additional non-climatic noise. The non-climatic noise is generated by adding white noise to the perfect pseudo-proxies. The amplitude of the white noise is defined such that the correlation between the noisy and the perfect pseudo-proxies is 0.5, i.e. the amplitude of the white noise corresponds to the standard deviation of the perfect pseudo-proxy times $\sqrt{3}$. This is a reasonable choice, as the correlation for real proxies with observations ranges from 0.3 to 0.7. The amount of white noise applied here is also well within the range of other pseudo-proxy studies (e.g. Smerdon, 2012). To ensure that the performance with noisy data is independent of the specific noise realisation, we create an ensemble of 30 noise realisations. In both TCppp and TCnpp we assume that all records are available at every point in time, i.e. that the network size remains constant in time. In reality, different proxy records cover different periods and the network size is not constant (Fig. 1b). Therefore, we set up a third test case (TCp2k) with realistic temporal proxy availability from the PAGES2k database and both perfect and noisy pseudo-proxies. In all three test cases, the pseudo-proxy records have annual resolution. The reconstruction period corresponds to the last 500 simulation years for TCppp and TCnpp, and to the entire 2000 simulation years for TCp2k.

To test the sensitivity of the method to the underlying climate-model simulation, we repeat the test cases TCppp and TCnpp with an analogously derived set of 25 pseudo-proxies and AMVI from simulations with the Community Climate System Model (CCSM4; Gent et al., 2011). We combine the "past1000" simulation (Landrum et al., 2013; Otto-Bliesner, 2014) and one "historical" simulation (Gent et al., 2011; Meehl, 2014) from the CMIP5 suite and use the last 500 years of the combined dataset. From the historical simulations, we used the ensemble member r1i1p1. The results are displayed in Appendix B.

2.2 Benchmark reconstruction

To have a benchmark for the GPR-based reconstruction in the cases of TCppp and TCnpp, we use pseudo-reconstructions with a multi-linear principal component regression (PCR). PCR is well established as a climate-index reconstruction method and has been used, for example, for reconstructions of the global mean surface temperature (PAGES2k, 2019) and the AMVI (Gray et al., 2004; Wang et al., 2017). The selected proxy time series are first decomposed into principal components (PCs); the latter are then used as predictors in a linear least-squares regression to obtain the AMVI for

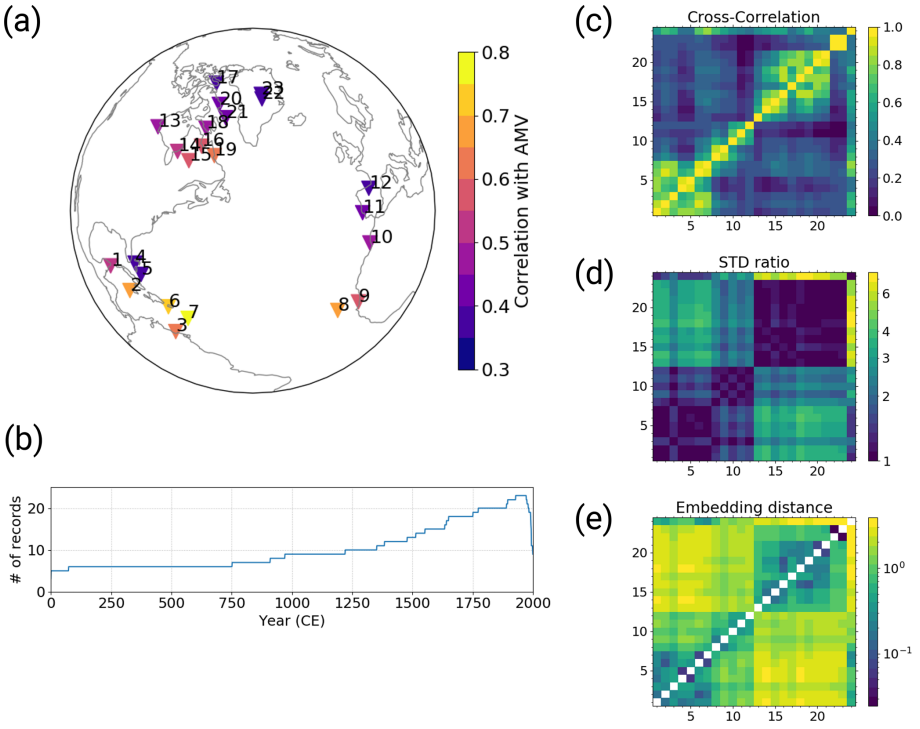

Figure 1. The selected pseudo-proxy records and resulting distance metrics based on the MPI-ESM simulation: **(a)** the locations of the records, colour-coded with the correlation between the records and the AMVI during the last 150 simulation years (after detrending); **(b)** the number of available proxy records at the selected locations within the PAGES2k dataset over time; **(c)** cross-correlation; **(d)** standard deviation ratio; and **(e)** the resulting embedding distances from the combination of both. Matrix indices 1–23 are the selected pseudo-proxy records as labelled in **(a)**, and index 24 is the simulated AMVI. The diagonal entries in **(e)** are empty because zero cannot be displayed on the logarithmic colour scale.

those time steps where proxies and AMVI overlap. In other words, the AMVI is expressed as a function of PCs of the original proxies (Eq. 1). We do not use all PCs but only retain those with a cumulative explained variance of 99.5 %. The trained model can then be used to reconstruct the AMVI for time steps where we have only proxies available:

$$\mathrm{AMVI}(t) = f_{\mathrm{PCR}}(\mathrm{PC}_1(t), \ldots, \mathrm{PC}_n(t)). \quad (1)$$

2.3 Gaussian process regression

2.3.1 The concept

Gaussian process regression is a Bayesian, non-parametric, supervised learning method (Rasmussen and Williams, 2006). Just like a probability distribution describes random variables, a Gaussian process (GP) describes a distribution over functions with certain properties. A GP is determined by a mean function and a covariance function:

$$f(\boldsymbol{x}) \sim \mathrm{GP}(\mu(\boldsymbol{x}), k(\boldsymbol{x}, \boldsymbol{x}')). \quad (2)$$

The mean function $\mu(\boldsymbol{x})$ describes the mean of all functions within the GP at location $\boldsymbol{x}$. In the absence of other knowledge, it is typically assumed that the mean of all functions within the prior GP is zero everywhere. The covariance function $k(\boldsymbol{x}, \boldsymbol{x}')$ describes the statistical dependence between the function values at two different points in the input space. The exact covariance structure is prescribed by a kernel function. Kernel functions range from very simple (e.g. linear, radial basis functions) to more complex (e.g. Matern functions, periodic). In principle, there is no limit to the kernel complexity and finding the right kernel can be considered an art in itself (e.g. Duvenaud et al., 2013). Once a general functional form of the kernel has been chosen (e.g. radial basis function), the specific form is determined by the kernel parameters. Since the underlying GP model itself is non-parametric, kernel parameters are often also referred to as hyperparameters (Rasmussen and Williams, 2006). These hyperparameters are either prescribed a priori, if they are known, or learned from the data through optimisation if they are unknown (e.g. through maximum likelihood estimation).

Without being constrained by data, the prior GP is a distribution of all functions with the given mean and covariance (Eq. 2). In order to use the GP for regression and prediction, the prior GP is combined with the additional information from the training data through the Bayes theorem (see Appendix A and Rasmussen and Williams (2006) for a more detailed description). Thus, the posterior GP is obtained, i.e.

only those functions are selected that agree with the training data in a given uncertainty range. Predictions at previously unseen input points are then given by that posterior distribution of functions evaluated at those unseen input points.

2.3.2 Finding the right regression space

As described for the PCR, classical climate-index reconstruction methods formulate their underlying statistical model so that the climate index is assumed to be a function of temperature, the proxy values or, for example, the principal components thereof. In other words, the regression is performed in temperature/proxy/PC space; the proxies/PCs are the predictors and the climate index is the predictand. If we reconstruct the AMVI with GPR in this classical setup, the target AMVI becomes the posterior mean function and the covariance is estimated across the proxy space. With the trained GP model, the AMVI can be reconstructed by evaluating the GP at the proxy values that occurred during the reconstruction period. Figure 2a shows the regression in proxy space for an example where the AMVI is given as a function of two pseudo-proxy records p_1 and p_2. In this example, the posterior mean AMVI function forms a surface in the space spanned by p_1 and p_2. (Note that in our pseudo-proxy experiments we use 23 pseudo-proxies (Fig. 1a), so the proxy space is actually 23-dimensional, which is impossible to visualise.)

In initial tests, the GPR reconstruction in proxy space did not perform well: the variability of the AMVI was strongly underestimated (not shown). A possible explanation is that GPs are very good interpolators but bad at extrapolating to regions of the proxy space that have not been sampled during training (e.g. upper left and lower right quadrants in the example of Fig. 2a) or where predictors become sparse (lower left quadrant in Fig. 2a). In those cases, the GPR estimation will fall back to the prior mean function (regression to the mean) and the predictive skill becomes very small. From a mathematical point of view, this setup of the regression in proxy space is also actually not suitable for GPR. Real-world proxies come with large uncertainties, and while GPs are designed to handle uncertain targets, they assume that the inputs are without uncertainty. Therefore, we approach the problem differently and set up the GPR in a way that leverages two GPR strengths: (1) being good interpolators and (2) handling uncertain targets.

In our new approach, we embed the entire available dataset (the selected pseudo-proxy records and AMVI at all points in time where observations are available) in a virtual space. The cloud of data points can be viewed as a sequence of images in this virtual space. The images contain missing values at time steps where we do not have AMVI observations available. The climate-index reconstruction problem thus becomes similar to an image-reconstruction problem. The GPR reconstructs the AMVI by filling the missing values based on the surrounding proxy values. In this framework, the GPR inputs are the locations in the embedding space and the GPR targets are the temperature anomalies of the proxies and the AMVI:

$$\Delta T_i = f_{\mathrm{GPR}}(t, \boldsymbol{x}_i), \tag{3}$$

where ΔT_i is either a proxy record p_i or the AMVI, and $\boldsymbol{x}_i$ is the location of the respective record within the embedding space. Figure 2b shows this embedding space for the example with two pseudo-proxies and the AMVI. The location of each time series within the embedding space is constant, so that the temporal sequence of data of one particular time series forms a straight line parallel to the time axis. The location of each record is based on its similarity to all other records. The more similar two records are, the closer they are located in the embedding space. To adequately reflect the distances between the proxy records and the AMVI, the embedding space needs to have a dimension of $(q-1)$, where q is the number of time series including the AMVI time series. This is easiest to understand if one imagines the case where all time series have the same distance from each other (as shown in Fig. 2b). To arrange, for example, three time series with equal distances from each other, one needs a two-dimensional space (spanned by x_1 and x_2 in Fig. 2b). In the case of the MPI-ESM-based proxy network, the embedding space has thus 23 dimensions (23 proxy records and 1 AMVI). With time as an additional dimension, the resulting space has a total of 24 dimensions. In the following, we will use $\boldsymbol{r}$ to refer to a point in space and time, and $\boldsymbol{x}$ and t to refer to points in only space and only time, respectively.

We then use the GP to find a function that fits the entire dataset in this virtual space and to interpolate the AMVI at the virtual locations $\boldsymbol{x}_{\mathrm{AMV}}$ for points in time where we do not have observations. With the right kernel formulation (see Sect. 2.3.4), we can account not only for cross-correlations between the different time series but also for temporal autocorrelation: a data point in the embedding space at time t_m is affected by all other surrounding points in the embedding space at time t_m and to a smaller extent also at times $t_n > t_m$ and $t_k < t_m$. The degree of influence is determined by the distance between the points in the embedding space and the typical length- and timescale of the kernel function. The closer two points are, the larger their influence.

Thus, the AMVI is still reconstructed based on the information from the pseudo-proxies, but we have formulated the problem such that the GP can handle the proxy-related uncertainty correctly, because the pseudo-proxies are now targets and no longer inputs. An additional advantage is that we can use this setup with variable proxy availability in time without having to retrain the model each time the proxy availability changes. Instead, the "images" simply have more missing values as the number of proxies decreases further back in time.

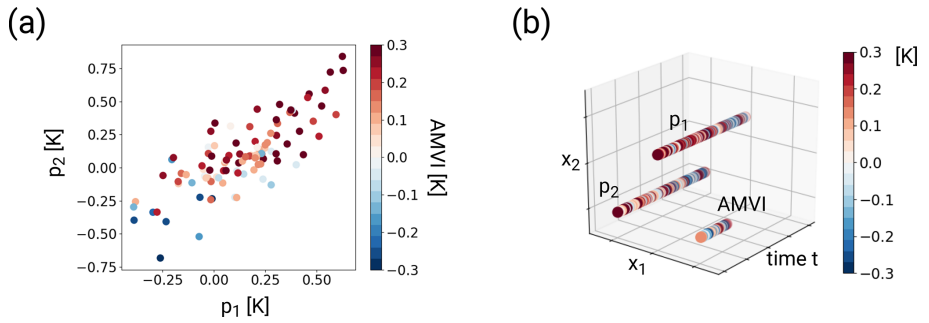

Figure 2. Schematic visualisation of the regression spaces for an example with two proxy records p_1 and p_2 and the AMVI. Panel **(a)** shows the GPR in the proxy space: the independent variables are the temperature anomalies of the proxy records; the dependent variable is the AMVI (colour coded) Panel **(b)** shows the GPR in the embedding space: the independent variables are the locations in the embedding space and time, and the dependent variables are the temperature anomalies of the proxy records and the AMVI (colour coded). In this simplified example, the three time series are located such that the distance between them is equal for all respective pairs of records.

2.3.3 Defining the distance matrix

Finding the right position $\boldsymbol{x}$ for each proxy record and the target index in the embedding space is an important and non-trivial step. Since we care only about the relative distance in the embedding space and not the absolute location, we can specify the distance between each pair of q records (proxies and AMVI) in a distance matrix $\mathbf{D}$ and determine the coordinates via multi-dimensional scaling (MDS; e.g. Mead, 1992). MDS uses the information of dissimilarity between objects to place these objects in a Cartesian space of a given dimension, such that the distance between the objects in the new space reflects the dissimilarity in an optimal way. In our case, the objects are the proxy records and the AMVI, and the given dimension is 23.

We define the distance matrix based on an appropriate distance metric. This could in principle be any distance metric such as the Euclidian distance or similar. To be used as a distance metric in MDS, a metric must meet the following three criteria: it needs to be (1) positive, (2) zero when it is applied on the object with itself and (3) symmetric (e.g. Mead, 1992). We chose to define the distance based on the cross-correlation (CC; Fig. 1c) and the standard deviation ratio (SR; Fig. 1d) of the respective records. The SR of two time series p_i and p_j is defined as

$$\mathrm{SR}_{ij} = \begin{cases} \frac{\mathrm{std}(p_i)}{\mathrm{std}(p_j)}, & \text{if } \mathrm{std}(p_i) > \mathrm{std}(p_j) \\ \frac{\mathrm{std}(p_j)}{\mathrm{std}(p_i)}, & \text{if } \mathrm{std}(p_i) < \mathrm{std}(p_j). \end{cases} \tag{4}$$

This way, the SR is symmetric, fulfilling the third criterion for the distance metric. Assuming that the records are all positively correlated, the distance measure between two time series p_i and p_j is defined as

$$D_{ij} = (1 - \mathrm{CC}_{ij}) \cdot \mathrm{SR}_{ij}, \tag{5}$$

i.e. the distance will be small when the CC is high and the records have similar amplitudes of variability, and larger when the CC is low and/or the records have very different amplitudes of variability (Fig. 1e). This choice of distance metric outperforms equidistant coordinates and a metric based solely on CC (not shown). With equidistant coordinates all records determine the AMVI to the same degree, regardless of their actual similarity to the AMVI. With a metric based solely on CC, the reconstruction is dominated by records with high variability and the resulting AMVI variability is overestimated. The additional SR scaling yields improved variability estimates.

The final distance matrix $\mathbf{D}$ is then obtained by evaluating Eq. (5) for all pairs of records. For all pairs of pseudo-proxies, the distance is estimated from the entire simulation length. For calculating the distance between the AMVI and the pseudo-proxies, we use only the last 150 years (years 1850 to 2000) and linearly detrend both AMVI and pseudo-proxies before the calculation. The so-determined unitless distances range from 0.02 to 3.91 for the MPI-ESM-based network (Fig. 1e). The resulting distance matrix is then used as input for the MDS algorithm to obtain the coordinates in a 23-dimensional space. The embedding distance reflects the actual geographical distance to a certain degree. Records that are close in actual space tend to be close also in the embedding space, as they have higher cross-correlations and similar standard deviations (Fig. 1e).

2.3.4 Kernel design and hyperparameters

We choose a very simple kernel function, the radial basis function (RBF), because we have no prior information that would justify the use of a more complex kernel. Complex kernels would introduce additional uncertainty and reduce the interpretability of the results. We define the kernel as an additive kernel of two RBF components:

$$k1(t_i, t_j) = \sigma_{\mathrm{f,t}}^2 \exp\left(\frac{1}{2}\left(\frac{|t_i - t_j|}{l_{\mathrm{f,t}}}\right)^2\right) \quad (6)$$

$$k2(\boldsymbol{r}_i, \boldsymbol{r}_j) = \sigma_{\mathrm{f,r}}^2 \exp\left(\frac{1}{2}\left(\frac{|\boldsymbol{r}_i - \boldsymbol{r}_j|}{l_{\mathrm{f,r}}}\right)^2\right). \quad (7)$$

The final kernel or covariance equation is then given as

$$k = k1 + k2. \quad (8)$$

In Eqs. (6) and (7), $|*|$ is the Euclidian distance between two points t_i and t_j or $\boldsymbol{r}_i$ and $\boldsymbol{r}_j$. The l_f and σ_f^2 are the hyperparameters of the respective kernels. l_f denotes a typical length scale of the target function, while σ_f^2 describes the signal variance, e.g. a function with small l_f and large σ_f^2 will be very wiggly.

The first kernel $k1$ operates on the time dimension only, i.e. it controls how much the neighbouring time steps at one embedding location influence the value at time t_j. This could be considered as a mean typical timescale of variability in the dataset. The second kernel $k2$ operates on all dimensions of the embedding space, including the time dimension. This enables interaction between locations at time t_j and neighbouring time steps. This kernel setup outperforms a kernel that consisted only of $k2$ and one where $k2$ did not include the time dimension (not shown). The higher skill of this kernel makes sense if one considers how the kernel design affects the interactions between the different time series. Having only $k2$ does not consider that the timescale of auto-correlation may not be the same as the timescale of cross-correlation. It therefore makes sense to have $k1$ operate across the time dimension only. If $k2$ operated only across the embedding dimensions, no interaction between different records across time would be possible.

Because $k2$ operates on both the time and the embedding dimensions, we rescale the time steps to be of the same order of magnitude as the distances between the records. This is necessary to allow for the interaction across records and time. Otherwise, the length scale of $k2$ would either be dominated by the time step or by the embedding distance. One rescaled time step equals the mean of the distance matrix $\mathbf{D}$. In the case of the MPI-ESM-based network (Fig. 1), the mean of the distance matrix is 1.44. For the CCSM-based network (Fig. B1), the mean of the distance matrix is 1.10.

A third additional hyperparameter σ_n^2 denotes the likelihood or noise variance (see also Appendix A). The noise variance enables the GPR to handle target uncertainty. A small σ_n^2 indicates that the targets have low uncertainty and the fitted function will be very strongly constrained by the training data. If σ_n^2 is larger, the targets come with large uncertainty. The fitted function is then less constrained by the training data and more robust against overfitting. Introducing σ_n^2 is similar to the so-called nugget effect in geostatistics. The noise variance σ_n^2 is assumed to be the same across all dimensions, i.e. the learned estimate will be the same for all pseudo-proxies and the AMVI. This is a simplification, because every pseudo-proxy contains its own level of noise. We will show that this simplification is a good first approximation and enables the GPR to handle uncertain pseudo-proxies well.

2.3.5 GP scaling behaviour

One known drawback of GPs is a bad scaling behaviour of the computing time required to estimate the hyperparameters with respect to the number of available observations, also called batch size. The training time of a GP scales with n^3, where n is the batch size. This is mainly due to the necessity to invert the covariance matrix (e.g. Rasmussen and Williams, 2006). Regression problems with more than 1000–10 000 observations become difficult to handle with the original GP formulation (hereafter full GP) due to time and computing memory limitations. Even though paleodatasets are not what we would typically call *big data*, they can already become challenging for GPs if the reconstruction period spans 1000 years or more.

Various GP variants have been proposed to overcome this limitation (e.g. Särkkä, 2013; Hensman et al., 2013). One variant is the so-called *stochastic variational GP* (SVGP; Hensman et al., 2013). The SVGP combines stochastic gradient descent (i.e. training with mini-batches), variational inference (i.e. inference through optimisation) and a low-rank approximation of the covariance matrix based on so-called inducing points. Simply put, the inducing points are a small subset of the original dataset that represents the properties of the complete dataset. In other words, the true GP posterior is approximated by a GP that is conditioned on the inducing points. The location of the inducing points in input space can either be prescribed manually (e.g. randomly) or they can be optimised along with the kernel hyperparameters. The training time of the SVGP scales with m^3, where m is the number of inducing points (Hensman et al., 2013). Here, we test both the full GP and the SVGP for climate-index reconstruction in the embedding space. In the following, we will refer to the embedded full GP as full emGP and the embedded SVGP as sparse emGP.

2.3.6 Technical notes

Our scripts are based on the Python package GPflow (Matthews et al., 2017). The hyperparameters are learned through optimisation with the Adam Optimiser, which is a stochastic gradient descent algorithm widely used in machine learning applications (Kingma and Ba, 2014). We use the algorithm as provided by GPflow. For the full GP, we repeat the optimisation step 1000 times. For the sparse GP, we initialise the inducing points as every tenth point in time and then optimise the locations along with the hyperparameters. We use mini-batches with a size of 2000 and repeat the optimisation

step 4000 times. The respective number of optimisation steps is sufficient for the estimated likelihood of reaching an equilibrium.

2.4 Training and testing

In the real world, SST measurements have been available only since approximately 1850; therefore, AMV observations also only have been available since then. We use this criterion to divide our pseudo-dataset into training and testing data. The relationship between the pseudo-proxies and the simulated AMVI can be inferred only from the last 150 years of the simulation, and the remaining years of the simulated AMVI are used for testing. This may not be the most effective way of splitting a dataset in the machine learning context, but it reflects best the actual data availability in the paleocontext.

For the benchmark PCR reconstruction, which takes place in the PCR space, the training inputs are the most recent 150 years of the retained principal components and the training targets are the corresponding 150 years of simulated AMVI (i.e. 1850–2000). In the testing period, the AMVI is reconstructed with the trained regression model and the remaining 350 years of the retained principal components as inputs.

For the emGPR reconstructions, the training inputs are the locations $\boldsymbol{r}_i$ of the pseudo-proxies and the AMVI. For the pseudo-proxies, all time steps are used for training (i.e. years 1500–2000); for the AMVI only the time steps corresponding to the last 150 simulation years are used for training (i.e. 1850–2000). The training targets are the corresponding values of the 23 proxy records p_i over the full 500 years and the AMVI record over the last 150 years. During training, the kernel hyperparameters and the noise variance are learned. The AMVI is then reconstructed by evaluating the trained emGP at the embedding location of the AMVI $\boldsymbol{x}_{\mathrm{AMV}} = \boldsymbol{x}_{24}$ and the time steps corresponding to the remaining 350 simulation years. This approach has the additional advantage that the training set is much bigger than in the classical setup. Thus, we increase the range of climate variability seen during training and reduce the risk of reconstructing climate states with which the model has not been trained.

3 Pseudo-reconstructions

3.1 TCppp: perfect pseudo-proxies

With perfect pseudo-proxies, the best overall reconstruction is achieved by the full emGPR. The reconstructed AMVI closely follows the target AMVI except for the period from approximately 1630 to 1680 (Fig. 3a). This is reflected by the high correlation with the target AMVI (0.93 for the smoothed index). There is a weak negative mean bias, corresponding to 20 % of the target standard deviation, which stems mainly from the 50-year period from 1630 to 1680. The GP related uncertainty, as given by the 95th percentile of the posterior distribution, is small for the years 1850–2000 where the AMVI has been constrained during training. The uncertainty increases for the reconstruction period. Overall, the posterior uncertainty estimate appears to be a bit too large – i.e. too conservative – because the true AMVI always lies within the 95 % confidence interval. The full emGPR captures the magnitude of variability very well. The standard deviation ratio of 0.93 indicates only a small underestimation of 7 %. Also, the period of very low AMVI following several volcanic eruptions between 1800 and 1850 is well captured, and the reconstructed and target AMVI are almost indistinguishable. The spectrum of the reconstructed AMVI agrees well with the spectrum of the target AMVI, and the full emGPR captures the variability at all frequencies (Fig. 3b).

The sparse emGPR captures the main features of the target AMVI, but the reconstruction is less accurate (Fig. 3c). The correlation is lower (0.79 for the smoothed index) and there are more periods with larger deviations between the reconstruction and the target. Interestingly, the sparse emGPR has large mismatches during different periods than the full emGPR. The full emGPR has the largest mismatch in the years 1630–1680 and the sparse emGPR has the largest mismatches in the years 1720–1830. The mismatches result in a positive mean bias corresponding to 33 % of the target standard deviation. The GP related uncertainty is the same as the uncertainty from the full emGPR, but in the sparse case, the uncertainty is approximately constant over the entire period. The standard deviation ratio is 0.80, i.e. the variability is underestimated by 20 %. This is, for example, visible for the years 1800–1850, where the very low AMVI is not captured as well as by the full emGPR. The spectrum of the reconstruction still agrees well with the target spectrum, but there is a slight overestimation of variability at the very high frequencies and an underestimation at lower frequencies at timescales of 80–100 years (Fig. 3d). Differences in the skill of the full and sparse emGP might partly be explained by different estimates of hyperparameters (see left halves of Fig. 5a–c). We assume that the hyperparameters learned with the full emGPR are closer to the truth. Both the estimated timescale of auto-correlation ($l_{\mathrm{f,t}}$) and the signal variance ($\sigma_{\mathrm{f,t}}$ and $\sigma_{\mathrm{f,r}}$) are underestimated by the sparse emGP.

The PCR reconstruction achieves the highest correlation (0.95 for the smoothed index) and comes with the smallest uncertainty range, but at the cost of a larger underestimation of variability and a systematic bias towards higher AMVI values, for periods during which the AMVI is outside of the range of the training period (Fig. 3e). This is especially apparent during the period of the very low AMVI from 1800 to 1850, where the target AMVI lies outside of the PCR uncertainty range. The mean bias corresponds to 79 % of the target standard deviation. The standard deviation ratio of 0.65 indicates an underestimation of the variability by 35 %. The underestimation occurs systematically at lower frequencies in

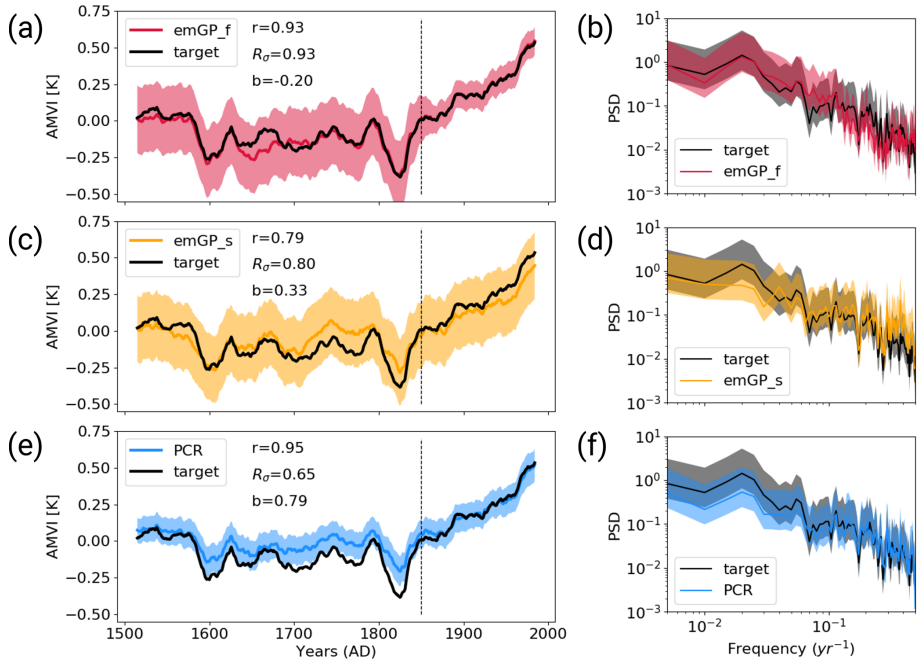

Figure 3. Reconstructions with perfect MPI-ESM pseudo-proxies based on **(a, b)** the full emGPR, **(c, d)** the sparse emGPR and **(e, f)** PCR. Panels **(a)**, **(c)**, **(e)** show the smoothed reconstructed and target time series. The dashed line marks the separation between training and testing periods. Shading indicates the 95 % confidence interval (CI). The CI is determined by the posterior GP distribution for the full and sparse emGP. For the PCR, the CI is derived from the uncertainty in the regression coefficients, which is based on the t distribution. The metrics r, R_σ and b denote correlation, the ratio of standard deviations and the bias relative to the target standard deviation, respectively. The metrics are calculated for the smoothed time series over the reconstruction period (1500–1850). Panels **(b)**, **(d)**, **(f)** show the Welch power spectra of the target and reconstructed AMVI. Shading indicates the 95 % confidence interval as obtained from the χ^2 distribution. The power spectral density (PSD) is given in K^2 per year.

the multi-decadal range, and the high-frequency variability (timescales shorter than 30 years) is well captured (Fig. 3f).

With CCSM4-based pseudo proxies, the results for the full and sparse emGPR are consistent with the MPI-ESM-based reconstructions (cf. Figs. 3a–d and B2a–d). The PCR performs much better in the CCSM environment, and both the underestimation of variability and the systematic bias to higher AMVI values are smaller in the CCSM4 case (cf. Figs. 3e and B2e). Also, the low-frequency variability is better captured (Fig. B2f). While the full emGPR clearly outperforms the PCR in the MPI-ESM case, PCR and the full emGPR perform similarly well in the CCSM4 case. The superior performance of the PCR in the CCSM4 case can be explained by a greater spatial coherence of the underlying CCSM4 temperature field. The leading EOF explains 41 % of the total variance in the CCSM4 case and only 27 % in the MPI-ESM case (not shown). The difference in spatial coherence is also reflected in the overall smaller embedding distances in the CCSM4 case (compare Figs. 1 and B1). The fact that the full and sparse emGPR perform about equally well for MPI-ESM and CCSM4 indicates that the emGPR is more robust to different degrees of spatial coherence in the underlying field. This can be considered an additional strength of the emGPR.

3.2 TCnpp: noisy pseudo-proxies

We calculate the reconstruction skill for each of the 30 noisy reconstructions separately and provide the mean and spread of the ensemble statistics. The distribution of the three skill metrics for each reconstruction method can be found in Appendix C. For the full emGP, the individual ensemble members are in reasonably good agreement with the target AMVI (see Figs. 4a and C1a). The mean correlation of the smoothed reconstructed AMVI with the target AMVI is 0.89 ± 0.06. The mean bias is with $21\,\% \pm 15\,\%$ of the target standard deviation, very similar to the bias from the TCppp case. As with the TCppp test case, the bias mostly stems from the years 1630 to 1680, where the mismatch between the reconstructions and target is largest. The variability is still captured remarkably well. The mean standard deviation ratio is 1.01 ± 0.17, indicating that most ensemble reconstructions contain a realistic amount of variability. The main loss of variability occurs at frequencies higher than decadal (Fig. 4b). The lower-frequency variability range, which is of main interest for studying the AMV, is well reconstructed, and the reconstructed spectra lie well within the uncertainty range of the target spectrum.

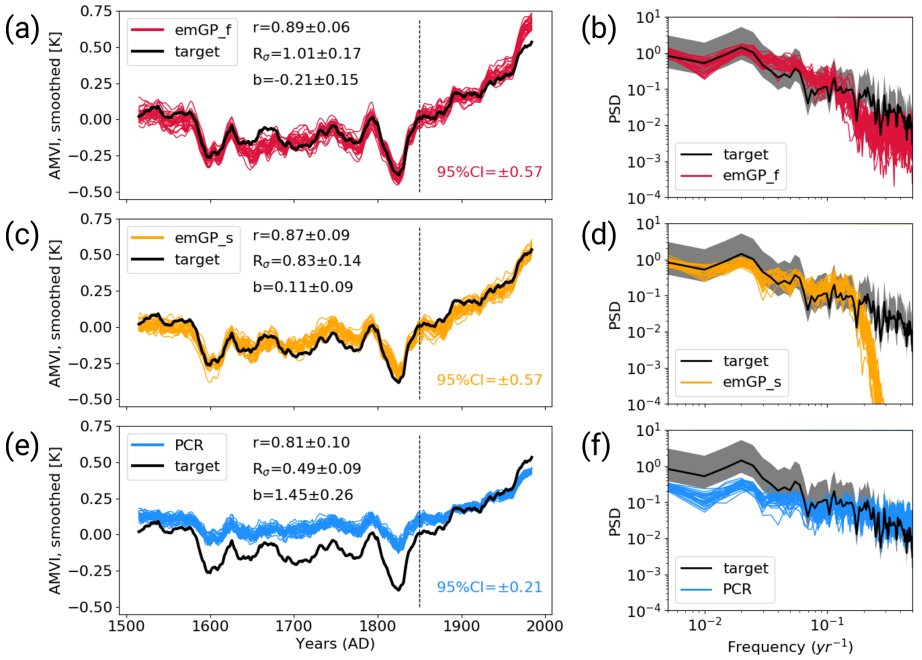

Figure 4. Reconstructions with noisy MPI-ESM pseudo-proxies based on **(a, b)** the full emGPR, **(c, d)** the sparse emGPR and **(e, f)** PCR. Panels **(a)**, **(c)**, **(e)** show the smoothed reconstructed and target time series. The dashed line marks the separation between training and testing periods. Thin coloured lines show the individual ensemble members. The 95 % CI in the lower right of all three panels indicates the CI averaged over time and all ensemble members. The metrics r, R_σ and b denote correlation, ratio of standard deviations and the bias relative to the target standard deviation, respectively. The metrics are calculated for each smoothed ensemble member over the reconstruction period (1500–1850), and the mean and spread ($\pm 2\sigma$) are reported here. Panels **(b)**, **(d)**, **(f)** show Welch power spectra of the target and reconstructed AMVI. Thin coloured lines indicate the spectra of the individual ensemble members. Grey shading indicates the 95 % CI of the target spectrum as obtained from the χ^2 distribution. The power spectral density (PSD) is given in K^2 per year.

The sparse emGPR also performs well with noisy pseudo-proxies (Figs. 4c, d and C1b). The overall reconstruction skill is even higher with noisy than with perfect pseudo-proxies. This improved performance is also reflected in the estimated timescale of auto-correlation. The estimate for $l_{f,t}$ is now much closer to the estimate from the full emGP (Fig. 5a; we will come back to this improved performance in Sect. 4). The ensemble mean correlation of the smoothed AMVI with the target AMVI is 0.87 ± 0.09. Also the mean bias is very small with 11 ± 9 % of the target standard deviation, only a third of the bias from the TCppp case. The mean standard deviation ratio is 0.83 ± 0.14, corresponding to an underestimation of the variability by $17\,\% \pm 14\,\%$. This underestimation is due to a complete loss of power at frequencies higher than decadal (Fig. 4d). But as with the full emGPR, the frequency range of interest for the AMV is well reconstructed.

The PCR still achieves high correlations but suffers a strong underestimation of variability and an increased systematic bias towards the mean of the AMVI over the training period (Figs. 4e, f and C1c). These deficiencies of the PCR reconstructions with noisy data have been well documented already (e.g. von Storch et al., 2009). The ensemble mean correlation with the smoothed target AMVI is 0.81 ± 0.10. The mean bias of $145\,\% \pm 26\,\%$ exceeds one standard deviation of the target AMVI. The mean standard deviation ratio is 0.49 ± 0.09, corresponding to an underestimation of variability by $51\,\% \pm 9\,\%$. The loss of variability occurs mainly in the range of frequencies *lower* than decadal, i.e. the frequencies of interest for the AMVI are severely underestimated (Fig. 4f).

The use of noisy pseudo-proxies has approximately doubled the width of the 95 % confidence intervals for all three methods. The mean uncertainty range over all emGP ensemble members is ± 0.57, which is again too conservative but reasonable given the amount of non-climatic noise in the pseudo-proxies. The mean PCR uncertainty range is ± 0.21, which is likely too confident in combination with the large reconstruction bias.

Again, the reconstruction results with the noisy CCSM4-based pseudo-proxies are broadly consistent with the MPI-ESM-based reconstructions (Figs. B3 and 4). Still, some notable differences occur. The full emGPR has a larger negative mean bias of $75\,\% \pm 17\,\%$ of the target standard deviation and slightly overestimates the variability on timescales longer than 80 years (Fig. B3a, b). The best reconstruction skill in the noisy CCSM4 case is achieved by the sparse emGPR, with high correlations, a small mean bias and a good estimation of the variability in the decadal to multi-decadal

frequency range (Fig. B3c, d). A possible explanation for the higher skill of the sparse emGPR can again be found in the hyperparameters. In the sparse case, the uncertainty from the noisy pseudo-proxies was correctly assigned to the noise variance σ_n^2 (Fig. B4c). In the full case, the large proxy noise was instead interpreted as signal variance ($\sigma_{f,r}$; Fig. B4b). We will return to this point in Sect. 4. With noisy pseudo-proxies, the PCR shows the same deficiencies as in the MPI-ESM case: a strong systematic bias towards the mean of the AMVI during the training period and a strong underestimation of variability on AMV-relevant timescales (Fig. B3e, f).

3.3 TCp2k: realistic PAGES2k proxy availability

Until now, we have assumed that the proxy availability is constant in time. In the following, we assess the reconstruction skill of the two emGPR methods with realistic – i.e. varying – data availability and over the full 2000 years. We do this in three steps: first, we test how the emGPR performs over the full 2000 years with perfect pseudo-proxies and constant data availability (i.e. the same as TCppp but over 2000 years). Second, we reconstruct the AMVI with perfect pseudo-proxies and realistically varying data availability. To achieve realistic data availability, we clip the annually resolved pseudo-proxy records at the start and end years of the corresponding real-world proxy records from the PAGES2k database. Third, we test the emGPR with noisy pseudo-proxies and varying data availability. The third step, even though still idealised, is closest to representing realistic conditions for proxy-based reconstructions.

Because the full and sparse emGPR differ in the amount of computing memory, we use two different approaches to reconstruct the full 2000 years. In our current computing environment and with the selected MPI-ESM-based proxy network of 23 locations, the full emGPR cannot handle much more than 500 years at a time. We therefore train the full emGPR on the most recent 500 years and use the estimated hyperparameters to reconstruct the AMVI piece-wise in the remaining three blocks of 500 years. For the first step, we actually take the hyperparameters from TCppp (red stars in Fig. 5). For the second step, we estimate the hyperparameters again to see how much they differ when the data availability changes (red diamonds in Fig. 5). For the full emGPR, they turn out to be very similar, and therefore we use the hyperparameters from TCnpp in the third step in order to save computing time (red dots in Fig. 5). The sparse emGPR can be trained and evaluated over the whole 2000 years at once with reasonable computational effort. Therefore, we retrain the hyperparameters in each of the three steps (yellow diamonds in Fig. 5).

3.3.1 Full emGPR

The first step with the full emGPR shows that our approach of piece-wise reconstruction works well. The reconstructed AMVI closely follows the target AMVI also in the years 0–1500 (Fig. 6a). This confirms that the hyperparameters estimated from the first 500 years are also representative of the remaining periods (at least in this MPI-ESM-based setting). The correlation of the smoothed reconstructed AMVI and the target AMVI is with 0.87, a bit lower as in the TCppp case. The mean bias of 8 % of the target standard deviation is smaller than in the TCppp case. The variability is well reconstructed, as indicated by both the standard deviation ratio of 1.03 and the power spectrum (Fig. 8a).

With variable data availability in the second step, the full emGPR still achieves a similarly high reconstruction skill (Fig. 6b). The correlation of the smoothed reconstructed AMVI and the target AMVI is 0.88 and the mean bias is negligible. Interestingly, the reduced data availability leads to an overestimation of variability in some periods (e.g. in the years 900–1100). This is also indicated by the standard deviation ratio of 1.19. This could be attributed to non-optimal hyperparameters for the reduced proxy availability in this period (see Sect. 4). The power spectrum also shows slightly higher power in the multi-decadal frequency range (Fig. 8b). On the other hand, there is a strong loss of power in the high-frequency range ($> 1/10$ per year).

The third step confirms that the full emGPR can achieve high reconstruction skill also under realistic conditions (Figs. 6c and C2a). The mean correlation of the smoothed AMVI reconstruction with the target AMVI is 0.67 ± 0.07 and the mean bias amounts to $12\,\% \pm 5\,\%$ of the target standard deviation. Many periods of extreme high and low AMVI are well captured (e.g. around years 300 and 1150), but some of these extreme periods are also underestimated (e.g. around year 550). The mean standard deviation ratio is 1.06 ± 0.15, indicating an overall realistic level of variability. Especially the variability in the decadal to multi-decadal range is still well captured (Fig. 8c). The only loss of variability occurs again in the high-frequency range on timescales shorter than decadal.

3.3.2 Sparse emGPR

In the first step, the sparse emGPR shows a slightly reduced reconstruction skill as compared with the TCppp case. The mean bias is very small, but the correlation is smaller and the underestimation of variability is stronger (Fig. 7a). The variability is underestimated both on interannual and multi-decadal to centennial timescales (Fig. 8d).

With variable data coverage in the second step, the reconstruction skill of the sparse emGPR remains similar and only the underestimation of variability on multi-decadal to centennial timescales increases (Figs. 7b and 8e).

In the third step, the mean correlation of the smoothed AMVI reconstructions with the target AMVI increases to 0.77 ± 0.07, confirming again that the sparse emGPR seems to capture some details of the AMVI better in the presence of noise (Figs. 7c and C2b), and the greater flexibility that

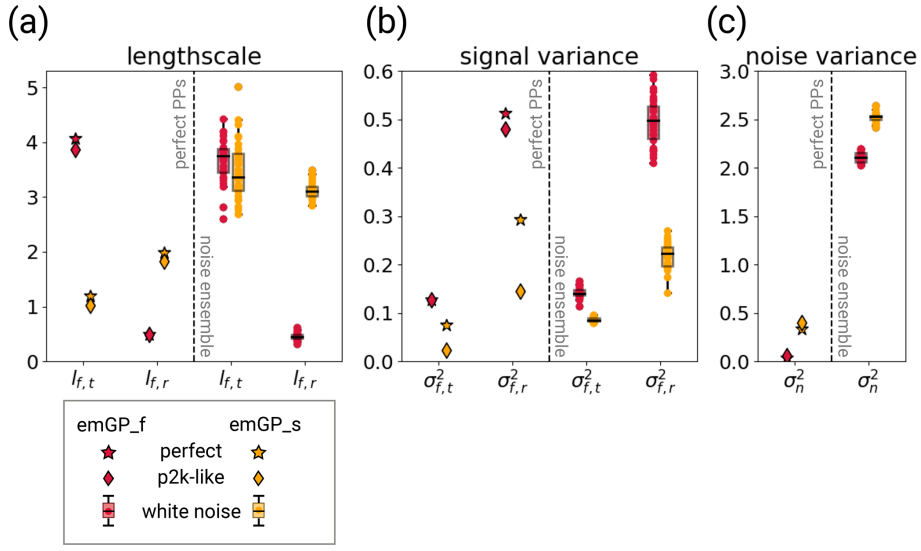

Figure 5. The hyperparameters of the two GPR versions for different training periods with perfect MPI-ESM pseudo-proxies (left halves of the panels) and the different white noise ensemble members (right halves of the panels). The hyperparameters are **(a)** the typical length scales $l_{f,t}$ and $l_{f,r}$, **(b)** the signal variance $\sigma^2_{f,t}$ and $\sigma^2_{f,r}$, and **(c)** the noise variance σ^2_n. The subscript t indicates that the kernel operates only on the time dimension. The subscript r indicates that the kernel operates on all dimensions, including time (see Eqs. 6 and 7). The length scales are unitless, corresponding to the unitless distance of the embedding space. The length scale $l_{f,t}$ can be transformed into years through division by 1.44. The signal and noise variance are given in K^2.

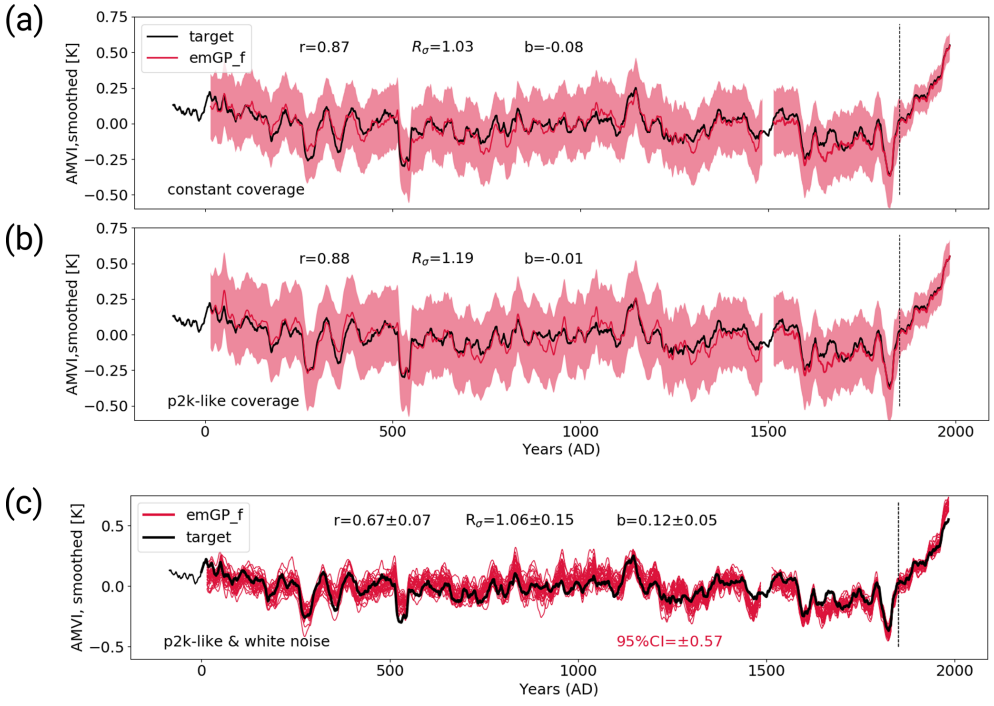

Figure 6. The MPI-ESM-TCp2k reconstructions with the full emGPR. Panel **(a)** shows the first step with perfect pseudo-proxies and constant proxy availability. Panel **(b)** shows the second step with perfect pseudo-proxies and realistic proxy availability according to the PAGES2k database. Panel **(c)** shows the third step with white noise added to the proxies and realistic proxy availability.

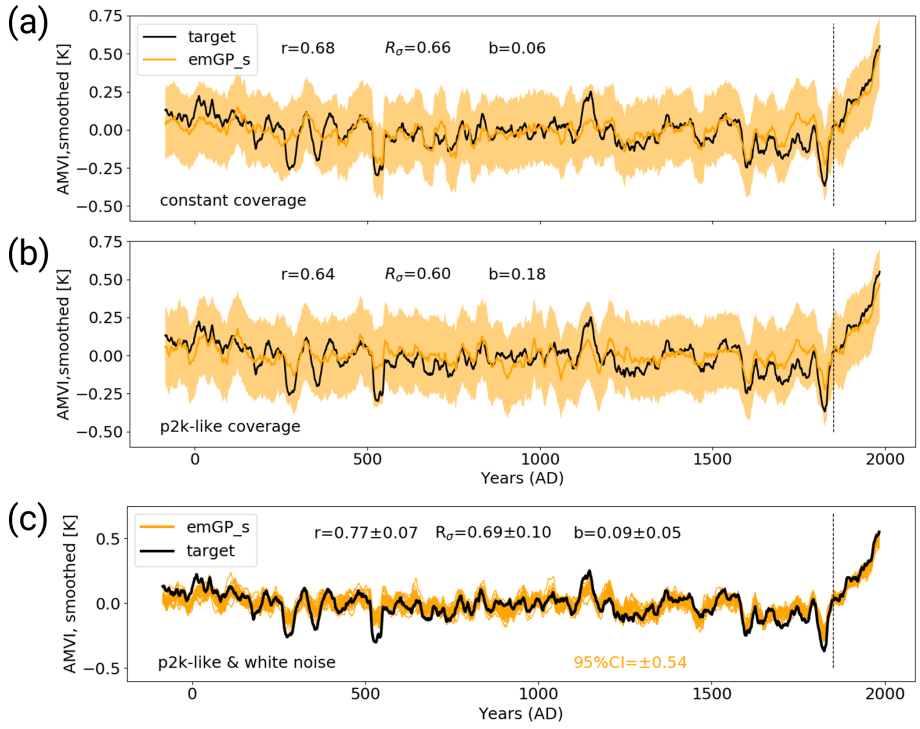

Figure 7. The MPI-ESM-TCp2k reconstructions with the sparse emGPR. Panel **(a)** shows the first step with perfect pseudo-proxies and constant proxy availability. Panel **(b)** shows the second step with perfect pseudo-proxies and realistic proxy availability according to the PAGES2k database. Panel **(c)** shows the third step with 3white noise added to the proxies and realistic proxy availability.

comes with a high estimate of noise variance in the GP hyperparameters (Fig. 5c). The underestimation of variability remains large, both on interannual and multi-decadal to centennial timescales (Fig. 8f). Even though the sparse emGPR obtains the worst reconstruction skill in this test case, the overall skill is still higher than that of the PCR with full data availability in the TCnpp case.

4 Discussion

We have tested two versions of GPR in a newly developed input space (embedding space) for climate-index reconstructions in pseudo-proxy experiments with increasingly realistic conditions. As a benchmark, we used a PCR-based reconstruction. Under perfect conditions (TCppp), all three methods – full and sparse emGPR and PCR – achieve high reconstruction skill. The full emGPR outperforms the sparse emGPR and performs at least as well as the PCR. With noise-contaminated pseudo-proxies (TCnpp), the full emGPR has the highest reconstruction skill with a realistic estimate of variability on AMV-relevant timescales (i.e. decadal to multi-decadal). The sparse emGPR achieves the second-best reconstruction skill with a realistic mean but increased variance loss. The PCR-based reconstruction is systematically biased to the AMVI values of the training period and suffers a strong loss of variance on AMV-relevant timescales. With realistic proxy availability and noise-contaminated pseudo-proxies (third step of TCp2k), the full emGPR is still able to achieve a high reconstruction skill with a realistic mean and variability on AMV-relevant timescales. Below, we re-assess the overall performance of the methods, give possible explanations for differences in reconstruction skill and discuss the wider applicability of the emGP.

4.1 Non-climatic noise

Our results indicate that the emGPR (both full and sparse) is able to perform well in the presence of non-climatic noise. This property can most likely be explained by the hyperparameter of the noise variance σ_n^2 (Fig. 5c). The noise variance describes the uncertainty in the regression targets. This concept can only be meaningfully applied here because we perform the GPR in the embedding space, where both the proxy time series and the AMVI are the regression targets. The noise variance can, therefore, capture the non-climatic signal of the pseudo-proxies and give the emGPR the necessary flexibility to filter the non-climatic part of the signal. Comparing the noise variance between the TCppp and TCnpp cases illustrates this quite well. In the TCppp case, the estimated noise variance (or likelihood) σ_n^2 lies between 0.1 and 0.4 K^2. In the TCnpp case, the estimated σ_n^2 lies between 2 and 2.7 K^2. This does reflect the actual mean magnitude of the noise which we added to the pseudo-proxies. The

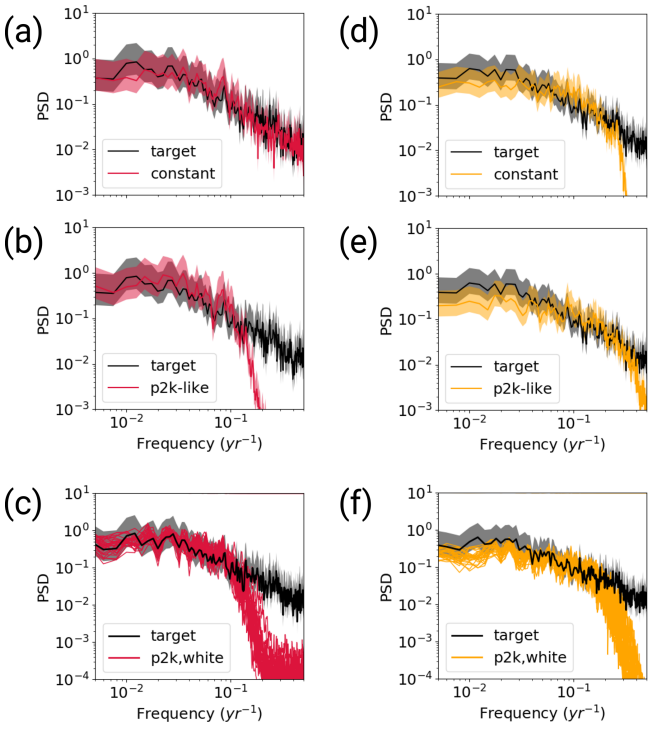

Figure 8. Welch power spectra of the MPI-ESM TCp2k reconstructions for the full (red) and sparse (yellow) emGPR. Panels **(a)**, **(d)** show the first step with perfect pseudo-proxies and constant proxy availability. Panels **(b)**, **(e)** show the second step with perfect pseudo-proxies and realistic proxy availability according to the PAGES2k database. Panels **(c)**, **(f)** show the third step with white noise added to the proxies and realistic proxy availability. Grey shading indicates the 95 % CI of the target spectrum. The power spectral density (PSD) is given in K^2 per year.

mean variance of the noise of all 23 records is approximately 2.1 K^2. (For the individual records, the variance of the added noise ranges from 0.3 to 4.9 K^2.) Thus, the GPR training procedure seems to be able to learn a realistic magnitude of the added noise.

Interestingly, the increased flexibility of the GP through the higher σ_n^2 not only yields robust reconstructions in the presence of uncertain pseudo-proxies, it also seems to improve the performance of the sparse emGPR. It is possible that the presence of noise makes the sparse emGP less sensitive to overfitting. To test this, we have repeated TCppp and TCnpp for the sparse emGP with a network consisting of only half the number of pseudo-proxies (randomly selected from the original networks). We would expect the difference in skill to decrease with the smaller networks, if overfitting was indeed the reason. The difference between the reconstruction with perfect and noisy data is indeed reduced with respect to the full networks (Fig. D1). The TCppp reconstruction has a comparable reconstruction skill to single TCnpp reconstruction members with both MPI-ESM and CCSM4-based pseudo-proxies. We therefore conclude that the improved performance of the sparse emGP with noisy data can at least partly be attributed to a greater robustness against overfitting in the presence of noise.

Here, we have only tested white noise pseudo-proxies, i.e. we assume that the noise in the pseudo-proxy records is not correlated in time. The typical noise model for σ_n^2, which we apply here, also works with the assumption of uncorrelated Gaussian white noise. For real proxies this may not always be the case. There are ways of adapting the noise model to include, for example, correlated noise (see Rasmussen and Williams, 2006). The embedding space would be a good starting point for this, as we explicitly take the time dimension into account. The noise model would introduce additional hyperparameters and make the calibration more complex. If we simply used our current setup with correlated noise, the model might interpret some of the noise correlation incorrectly as actual data correlation. This could be the subject of a follow-up study.

4.2 Hyperparameter estimation and overfitting

The full emGPR achieves generally higher reconstruction skill than the sparse emGPR. (One exception is the TCnpp case with CCSM4-based pseudo-proxies.) This could be expected, since the sparse emGPR approximates the covariance matrix based on only a tenth of the available training data, i.e the subset of selected inducing points. Possibly, the hyperparameters are more accurately learned from the full dataset. Another possibility is that the location of the inducing points is non-optimal. We have initialised the inducing points as every tenth step in time and then optimised the location during training. We have not tested other setups of the inducing points. It is possible that a higher number or differently selected inducing points would result in a higher reconstruction skill.

The optimisation of the hyperparameters is an additional source of uncertainty. The learned set of hyperparameters may not always be the optimal set. We did not make any sensitivity tests regarding, for example, initialisation of the hyperparameters. But the fact that the training of the full emGPR resulted in similar hyperparameters for all three MPI-ESM-based test cases (TCppp,TCnpp and TCp2k) gives us confidence that the estimated hyperparameters for the full emGPR are accurate. The hyperparameters that have a straightforward physical interpretation, i.e. the typical length scale $l_{f,t}$ and variance $\sigma_{f,t}^2$ of the first kernel and the noise variance σ_n^2, also appear reasonable in their magnitudes in most cases (red stars in Fig. 5). The timescale of the full emGP is on the order of 2.7 years, which is a reasonable timescale of auto-correlation. As discussed above, σ_n^2 captures the magnitude of the mean added noise variance across all records. The signal variance $\sigma_{f,t}^2 = 0.12\,K^2$ indicates a temporal temperature variability of approximately 0.35 K. For all selected pseudo-proxies, the temporal variability ranges from 0.28 to 1.15 K. The estimated $\sigma_{f,t}$ is thus on the lower end of plausi-

ble values. The timescale $l_{f,r}$ and variance $\sigma^2_{f,r}$ of the second kernel are less straightforward to interpret, as they operate across space and time. However, $\sigma^2_{f,r}$ should somehow reflect the mean temperature variability across all records and time. The estimate of $\sigma^2_{f,r} = 0.51\,K^2$ indicates a variability of 0.71 K. This is a fairly close estimate of the actual 0.82 K of the underlying data.

Based on the comparison of the hyperparameters across all experiments, we identify two possible cases of non-optimal hyperparameters: first, the TCppp case with the sparse emGPR, based on both MPI-ESM and CCSM4 pseudo-proxies, in which the estimated typical timescale $l_{f,t}$ is much shorter than that estimated from the full emGPR (left halves of Figs. 5a and B4a; and second, the TCnpp case with the full emGPR and CCSM4-based pseudo-proxies. In this case, the noise variance was not correctly estimated. Instead, the noise variance was attributed to the signal variance $\sigma^2_{f,r}$. The values of σ^2_n and $\sigma^2_{f,r}$ appear switched compared with the other TCnpp experiments (compare the right halves of Fig. 5b and c, and Fig. B4b and c). Repeating the CCSM4-based TCnpp experiment with switched σ^2_n and $\sigma^2_{f,r}$ slightly increases the reconstruction skill, but the skill remains lower than for the TCnpp with the sparse emGPR (not shown). This illustrates how difficult it is to find an optimal set of hyperparameters.

As with all reconstruction methods, it is possible that the (hyper)parameters learned during training are not completely representative for the reconstruction period. To test for the non-stationarity of hyperparameters in case of changing proxy availability, we have repeated the TCp2k experiment with the full emGP for the years 1000–1500 (Fig. D2). The new hyperparameters indicate a smaller signal variance and shorter auto-correlation timescale (red and grey diamonds in Fig. D3). This improves the reconstruction skill with respect to the original TCp2k experiment. However, non-stationary hyperparameters are difficult to account for with real-world data. By training the emGP with the maximum of available proxy data, we try to get the best mean estimate but cannot fully avoid the effect of non-stationarity.

4.3 Embedding distance

As well as the hyperparameters, also the embedding distances are not constant in time (Fig. D4). Changing cross-correlations may lead to under- or overestimation of individual records during certain periods. Again, this is something which is difficult to account for with real-world data, and by calculating the embedding distance over the entire periods of proxy availability we try to find the best mean distance estimate.

Another source of uncertainty is the choice of the distance metric on which the creation of the embedding space is based. We have tested equidistant coordinates, cross-correlation and cross-correlation with standard deviation ratio, and we selected the latter metric. But of course, other ways of constructing the embedding space could be possible. The optimal embedding space may differ for each proxy network and proxy properties. This is definitely worthy of further investigation.

4.4 Climate model dependence

The skill of all three methods, including the benchmark PCR, depends to some degree also on the climate model from which the pseudo-proxies are derived. This is a known issue (Smerdon et al., 2011). The full emGPR performs better in the MPI-ESM-based experiments, the PCR performs better in the CCSM4-based experiments and the sparse emGPR performs about equally well in both model worlds. The reason for the different skill could be the differences in the network size and location of the pseudo-proxies and differences in the cross-correlation structure. It is, of course, difficult to say whether a reconstruction with real proxies will behave more like the MPI-ESM-based experiments or more like the CCSM4-based experiments. But regardless of the differences in skill, the fact that the emGPR has higher reconstruction skill in the more realistic TCnpp case, and suffers from a much smaller variability loss than the PCR in both model worlds, gives us confidence that emGPR will also improve the reconstructed variability in a real reconstruction.

4.5 Using real proxies and wider applications

The pseudo-proxy experiments give a good first impression of how the reconstructions may behave with real proxies. Nonetheless, even though the third step of TCp2k (noise contamination and variable proxy coverage) is already quite realistic, it is still idealised. For example, in the pseudo-proxy setup, we calculate the distance matrix **D** based on the whole length of the simulation. With real proxies, each proxy record has a different length and covers a different period. In this case, the distance matrix could be calculated based either on a common time period where all records are available (this could be a very short period) or it could be the period of overlap for each individual pair of records.

In principle, the framework presented here can be applied to any climate index that exhibits significant correlations with local proxy sites. It is thus not limited to the AMVI application presented here. With real proxies, which do not all come in units of °C (e.g. lake sediments, tree ring width and isotope ratios), it might make more sense to standardise all records to unit variance. In this case, the embedding distance would no longer need to include the SR scaling. A simple dependence on the CC might be sufficient. This remains to be tested.

In order to use this framework for indices that operate on longer timescales, it might become necessary to include records with lower temporal resolution. This would require subsampling of all records to the lowest common resolution, which is common practice in long-term reconstructions. It might also be possible to train one emGP model for the high-

resolution records and one for the low resolution-records. The caveat here is that the observational period is often too short to include enough training data for the low-resolution records. But this is true for all reconstruction methods and not unique to the emGP framework here.

In the TCnpp cases, we created 30 different white noise realisations to estimate the noise-related uncertainty. With real proxies, we only have one realisation of the data, of course, and cannot run noise ensembles. But one could think of other ways of generating ensembles, e.g. with slightly different hyperparameters, slightly different ways of constructing the distance matrix or inclusion of different noise models for σ_n^2. This would instead give insight into the other more methodological sources of uncertainty.

5 Conclusions

We have developed and tested a new method for proxy-based climate-index reconstruction. Our aim was to reduce the underestimation of variability on AMV-relevant timescales (decadal to multi-decadal), which is a common drawback of established reconstruction techniques such as PCR. To this end, we applied Gaussian process regression and developed a modified input space, which we denoted as the embedding space. We tested two versions of GPR, a full version and a stochastic variational, i.e. sparse, version. The full version is generally more accurate but comes at high computational costs and can only handle a limited amount of data. As a benchmark comparison, we also computed AMVI reconstructions with PCR.

Under ideal conditions (TCppp: pseudo-proxies contain only the climate signal, all records available over the entire reconstruction period), the embedded full GPR performs at least as well as the PCR; in the pseudo-proxy experiments based on MPI-ESM the embedded GPR achieves an even higher reconstruction skill and suffers almost no variance loss. Under more realistic conditions (TCnpp: pseudo-proxies contaminated with non-climatic white noise, all records available over the entire reconstruction period), the reconstruction skill of the PCR strongly decreases, and both the embedded full and sparse GPR clearly outperform the PCR. The GP-based reconstructions have an overall small mean bias and reconstruct the variability on AMV-relevant timescales much more accurately. Under even more realistic conditions (TCp2k: pseudo-proxies contaminated with non-climatic white noise, records have different length and cover different periods), the embedded sparse GPR still has an overall small mean bias but suffers a strong variance loss, while the embedded full GPR is still capable of reconstructing the variability on the timescales of interest accurately.

Of course, it remains to be seen how the embedded GPR performs with real proxies. As a next step, we will perform a real AMVI reconstruction based on the PAGES2k proxy network. Based on the results presented in this study, we are confident that climate-index reconstructions can be significantly improved with embedded GPR. A more accurate reconstruction of the mean state and the magnitude of variability will help advance our understanding of AMV dynamics, e.g. especially during periods of extreme cooling following volcanic eruptions.

Appendix A: Calculating the posterior predictive distribution

Given a set of observed data $\boldsymbol{y} = y_i = f(\boldsymbol{x}_i)$, the objective is to provide the probability distribution at a yet unobserved data point z, $f(z)$, conditional on the available observations. This is achieved by the application of the Bayes theorem. Before the application of Bayes theorem, the prior for $f(z)$ is just the assumed probability distribution for the Gaussian process, with mean $\mu_{\text{prior}}(z)$ and variance $\text{cov}_{\text{prior}} = k(z,z)$. Usually, μ_{prior} is assumed to be zero without loss of generality (e.g. by taking anomalies from the mean). It is also assumed that observations are a realisation of a *noisy* Gaussian process, which are contaminated by uncertainty in observations, i.e, $y_i = f(\boldsymbol{x}_i) + \epsilon$. The noise ϵ is assumed to be Gaussian with variance σ_n^2 and uncorrelated across the locations $\boldsymbol{x}_i$. After the application of Bayes theorem, the mean and variance can be calculated according to the following predictive equations (for a detailed derivation see Rasmussen and Williams, 2006):

$$\mu_{\text{post}}(z) = k(z,\boldsymbol{x})^T [k(\boldsymbol{x},\boldsymbol{x}) + \sigma_n^2 \mathbf{I}]^{-1} \boldsymbol{y} \tag{A1}$$

$$\text{cov}_{\text{post}}(z) = k(z,z) - k(z,\boldsymbol{x})[k(\boldsymbol{x},\boldsymbol{x}) + \sigma_n^2 \mathbf{I}]^{-1} k(\boldsymbol{x},z), \tag{A2}$$

where $\mathbf{I}$ is the identity matrix. These equations can be interpreted as follows: the posterior mean is a linear combination of observations $\boldsymbol{y}$ and the process covariances between positions of the available observations and the new position $k(z,\boldsymbol{x})$. Usually, the kernel is assumed to decrease with increasing separation between locations. This implies that when the new position z is out of the range of available observations, the posterior mean will tend towards the prior mean. The posterior variance is smaller than the prior variance, since the available observations reduce the range of likely values of $f(z)$.

Appendix B: CCSM4 pseudo-proxies

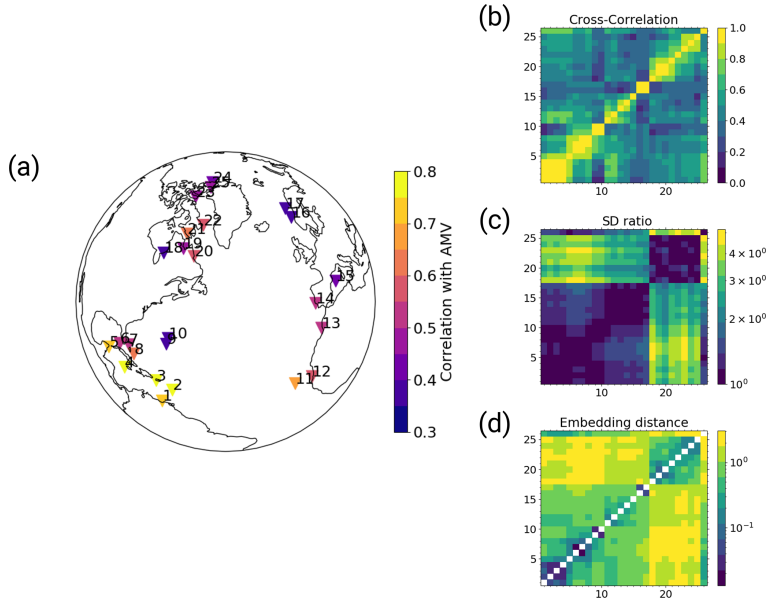

Figure B1. The selected pseudo-proxy records and resulting distance metrics based on the CCSM4 simulation: **(a)** the locations of the records, colour coded with the correlation between the records and the AMV during the last 150 simulation years (after detrending); **(b)** cross-correlation; **(c)** standard deviation ratio; and **(d)** the resulting embedding distances from the combination of both. Matrix indices 1–25 are the selected pseudo-proxy records as labelled in **(a)**, and index 26 is the simulated AMV index. The diagonal entries in **(d)** are empty because zero cannot be displayed on the logarithmic colour scale.

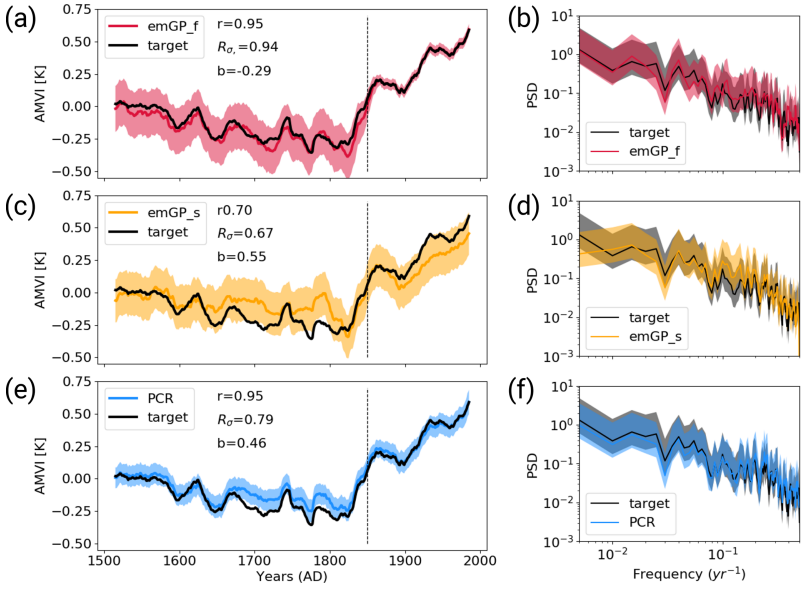

Figure B2. Reconstructions with perfect CCSM4 pseudo-proxies based on **(a, b)** the full emGPR, **(c, d)** the sparse emGPR and **(e, f)** PCR. Panels **(a)**, **(c)**, **(e)** show the smoothed reconstructed and target time series. The dashed line marks the separation between training and testing periods. Shading indicates the 95 % confidence interval. The metrics r, R_σ and b denote correlation, the ratio of standard deviations and the bias relative to the target standard deviation, respectively. The metrics are calculated for the reconstruction period (1500–1850). Panels **(b)**, **(d)**, **(f)** show the Welch power spectra of the target and reconstructed AMVI. Shading indicates the 95 % confidence interval. The power spectral density (PSD) is given in K^2 per year.

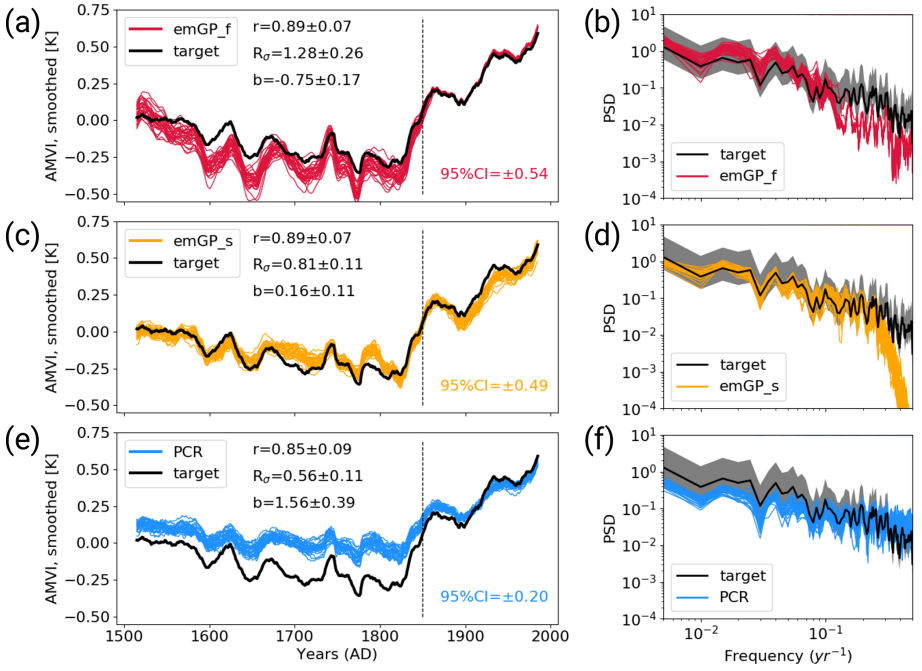

Figure B3. Reconstructions with noisy CCSM4 pseudo-proxies based on **(a, b)** the full emGPR, **(c, d)** the sparse emGPR and **(e, f)** PCR. Panels **(a)**, **(c)**, **(e)** show the smoothed reconstructed and target time series. The dashed line marks the separation between training and testing periods. Thin lines show the individual ensemble members and the bold line indicates the ensemble mean. The metrics r, R_σ and b denote correlation, ratio of standard deviations and the bias relative to the target standard deviation, respectively. The metrics are calculated for each smoothed ensemble member over the reconstruction period (1500 to 1850), and the mean and spread ($\pm 2\sigma$) are reported here. Panels **(b)**, **(d)**, **(f)** show Welch power spectra of the target and reconstructed AMVI. Thin lines indicate the spectra of the individual ensemble members and the bold line indicates the spectrum of the ensemble mean. Shading indicates the 95 % confidence interval of the ensemble mean spectrum. The power spectral density (PSD) is given in K^2 per year.

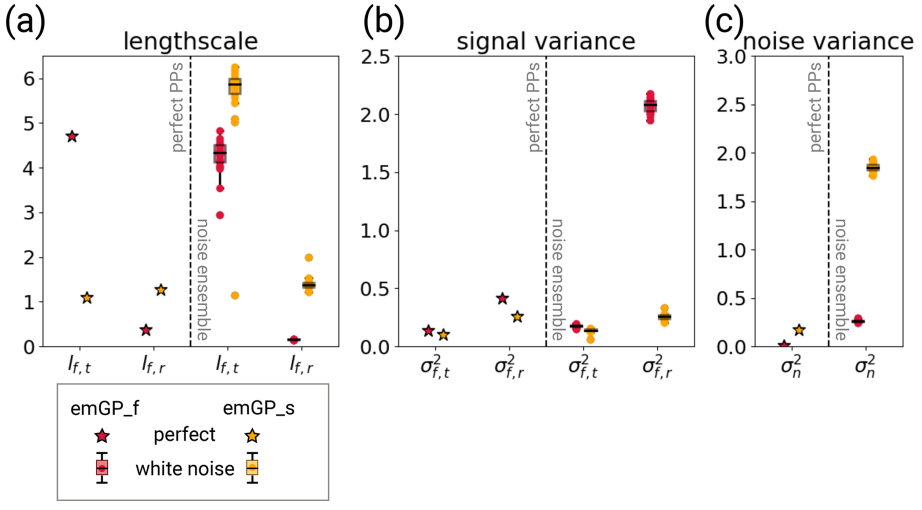

Figure B4. The respective hyperparameters for different training periods with CCSM4-based perfect pseudo-proxies (left halves of the panels) and the different white noise ensemble members (right halves of the panels). The hyperparameters are **(a)** the typical length scales $l_{f,t}$ and $l_{f,r}$, **(b)** the signal variance $\sigma^2_{f,t}$ and $\sigma^2_{f,r}$, and **(c)** the noise variance σ^2_n. The subscript t indicates that the kernel operates only on the time dimension. The subscript r indicates that the kernel operates on all dimensions, including time (see Eqs. 6 and 7). The length scales are unitless, corresponding to the unitless distance of the embedding space. The length scale $l_{f,t}$ can be transformed into years through division by 1.10. The signal and noise variance are given in K^2.

Appendix C: Metrics of TCnpp ensemble members

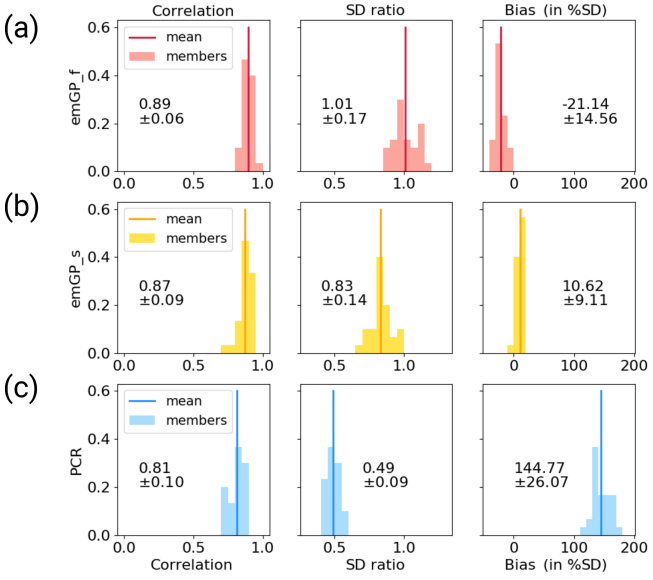

Figure C1. Distribution of skill metrics for the ensemble of reconstructions with noisy MPI-ESM pseudo-proxies with **(a)** the full emGPR, **(b)** the sparse emGPR and **(c)** PCR. The histograms show the respective distributions and the vertical lines indicate the ensemble mean. The printed values denote the mean and spread (2σ) which are also reported in the text and Fig. 4.

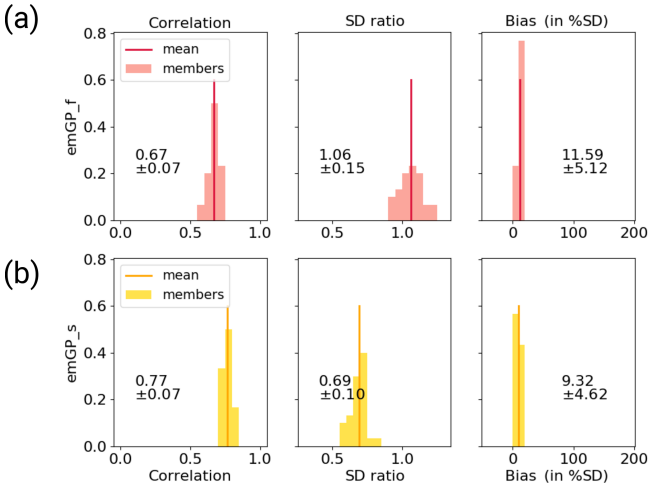

Figure C2. Distribution of skill metrics for the ensemble of reconstructions with noisy MPI-ESM pseudo-proxies and realistic data-availability with **(a)** the full emGPR and **(b)** the sparse emGPR. The histograms show the respective distributions and the vertical lines indicate the ensemble mean. The printed values denote the mean and spread (2σ) which are also reported in the text and in Figs. 6 and 7.

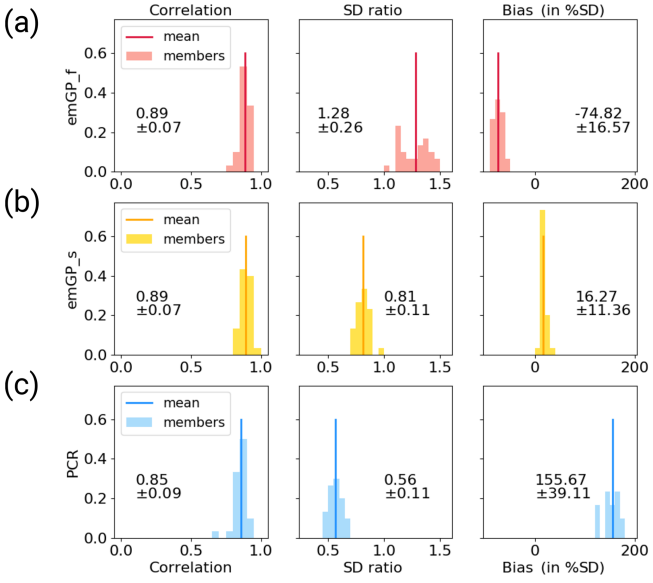

Figure C3. Distribution of skill metrics for the ensemble of reconstructions with noisy CCSM4 pseudo-proxies with **(a)** the full emGPR, **(b)** the sparse emGPR and **(c)** PCR. The histograms show the respective distributions and the vertical lines indicate the ensemble mean. The printed values denote the mean and spread (2σ) which are also reported in the text and Fig. B3.

Appendix D: Sensitivity experiments

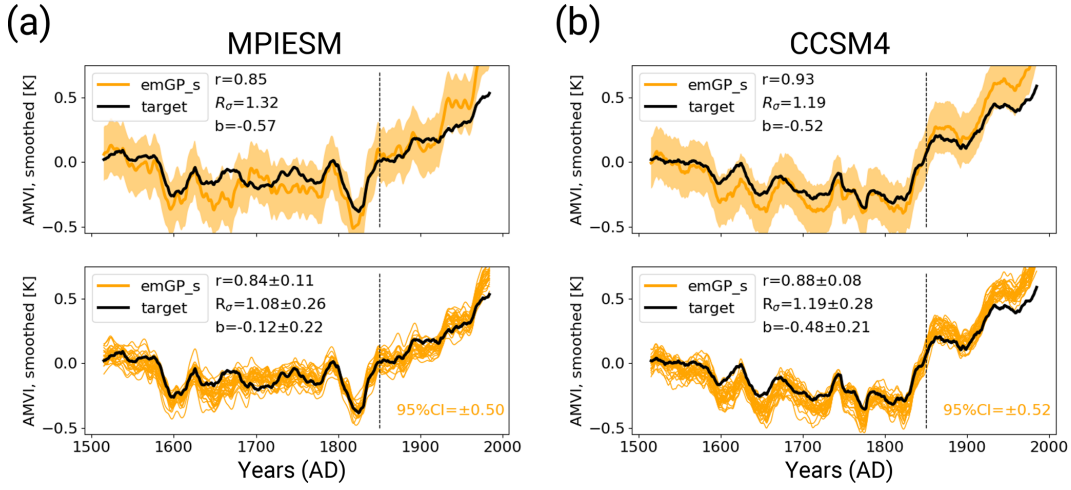

Figure D1. Sensitivity experiments similar to TCppp and TCnpp with the sparse emGP but with only half the number of pseudo-proxies. Reconstructions based on **(a)** 11 MPI-ESM-based pseudo-proxies and **(b)** 12 CCSM4-based pseudo-proxies. The upper panels show the reconstruction with perfect pseudo-proxies and the lower panels show the reconstruction with noisy pseudo-proxies.

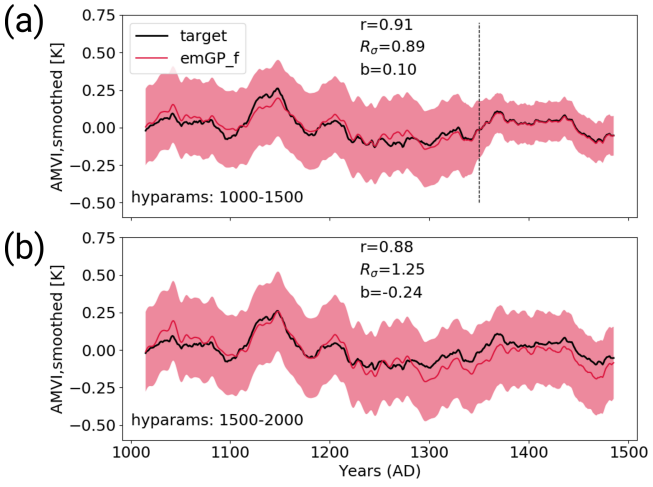

Figure D2. Panel **(a)** shows a sensitivity experiment similar to TCp2k with the full emGP, but the hyperparameters are estimated for the period 1000–1500, where the proxy availability is strongly reduced (see Fig. 1b). The AMVI during the years 1350–1500 has been used for training. Panel **(b)** shows AMVI reconstruction for the same period from Fig. 6b for comparison. Here, the hyperparameters were estimated for the period 1500–2000.

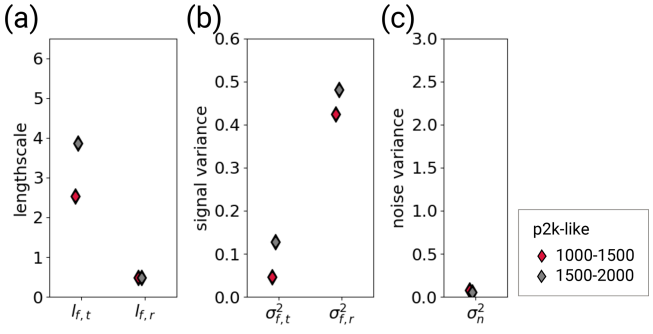

Figure D3. Hyperparameters of the sensitivity experiment shown in Fig. D2. Red diamonds correspond to the period 1000–1500 and grey diamonds to the period 1500–2000. (Grey diamonds here are the same as the red diamonds in Fig. 5.) The hyperparameters are **(a)** the typical length scales $l_{\mathrm{f,t}}$ and $l_{\mathrm{f,r}}$, **(b)** the signal variance $\sigma^2_{\mathrm{f,t}}$ and $\sigma^2_{\mathrm{f,r}}$, and **(c)** the noise variance σ^2_{n}. The subscript t indicates that the kernel operates only on the time dimension. The subscript r indicates that the kernel operates on all dimensions, including time (see Eqs. 6 and 7). The length scales are unitless, corresponding to the unitless distance of the embedding space. The length scale $l_{\mathrm{f,t}}$ can be transformed into years through division by 1.10. The signal and noise variance are given in K^2.

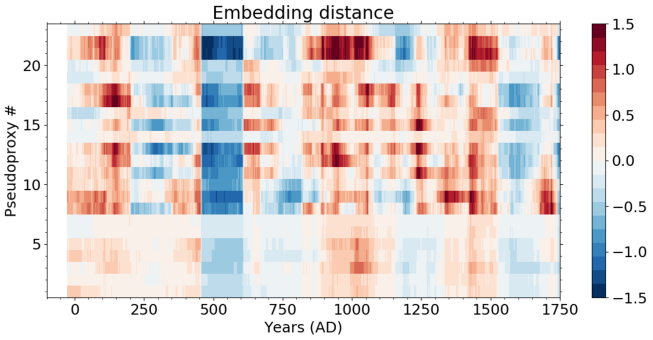

Figure D4. Changes in the embedding distance between the AMVI and the pseudo-proxy records (Eq. 5) calculated over a running window of 151 years. The anomalies are calculated against the mean distance over the entire period. Blue shading indicates a smaller distance, i.e. more similar records. Red shading indicates a greater difference, i.e. less similar records. The numbers on the *y* axis correspond to the pseudo-proxy numbering in Fig. 1.

Code and data availability. The extracted pseudo-proxy data and the simulated AMVI from the MPI-ESM and CCSM4 simulations, as well as the Python scripts for the preparation of the pseudo-proxy network, the preparation of the embedding space and the GP regression, are provided in the Supplement. The Python packages Scikit-learn (v.0.19.1), TensorFlow (v.1.12.0) and GPflow (v.1.3.0) are publicly available. The PAGES2k database can be downloaded at https://doi.org/10.6084/m9.figshare.c.3285353 (Kilbourne et al., 2017). The CCSM4 past1000 and historical simulations can be obtained from the World Data Center for Climate (https://doi.org/10.1594/WDCC/CMIP5.NRS4pk) (Otto-Bliesner, 2014) and https://doi.org/10.1594/WDCC/CMIP5.NRS4hi (Meehl, 2014), respectively.

Supplement. The supplement related to this article is available online at: https://doi.org/10.5194/gmd-17-1765-2024-supplement.

Author contributions. MK and EZ conceptualised the study. UvT developed the concept of the embedding space. MK implemented the code, performed the pseudo-reconstructions, analysed the results and wrote the first draft of the manuscript. All authors discussed the results and contributed to writing the paper.

Competing interests. The contact author has declared that none of the authors has any competing interests.

Disclaimer. Publisher's note: Copernicus Publications remains neutral with regard to jurisdictional claims made in the text, published maps, institutional affiliations, or any other geographical representation in this paper. While Copernicus Publications makes every effort to include appropriate place names, the final responsibility lies with the authors.

Acknowledgements. This study has been performed in the context of RedMod (https://redmod-project.de, last access: 22 February 2024). The emGPR reconstruction code was run on the gpu nodes of the supercomputer *Mistral* at the German Climate Computing Centre (DKRZ). The MPI-ESM simulation was run by Sebastian Wagner (Helmholtz-Zentrum Hereon). The analysis was enabled and facilitated by the open-source Python packages Scikit-learn (Pedregosa et al., 2011), TensorFlow (Abadi et al., 2015) and GPflow (Hensman et al., 2013). Figures were generated with Matplotlib (Hunter, 2007).

Financial support. This research has been supported by the Helmholtz-Gemeinschaft (Helmholtz-Inkubator-Initiative, Reduced Complexity Models grant).

The article processing charges for this open-access publication were covered by the Helmholtz-Zentrum Hereon.

Review statement. This paper was edited by Olivier Marti and reviewed by two anonymous referees.

References

Abadi, M., Agarwal, A., Barham, P., Brevdo, E., Chen, Z., Citro, C., Corrado, G. S., Davis, A., Dean, J., Devin, M., Ghemawat, S., Goodfellow, I., Harp, A., Irving, G., Isard, M., Jia, Y., Jozefowicz, R., Kaiser, L., Kudlur, M., Levenberg, J., Mané, D., Monga, R., Moore, S., Murray, D., Olah, C., Schuster, M., Shlens, J., Steiner, B., Sutskever, I., Talwar, K., Tucker, P., Vanhoucke, V., Vasudevan, V., Viégas, F., Vinyals, O., Warden, P., Wattenberg, M., Wicke, M., Yu, Y., and Zheng, X.: TensorFlow: Large-Scale Machine Learning on Heterogeneous Systems, https://www.tensorflow.org/ (last access 22 February 2024), 2015.

Barboza, L., Li, B., Tingley, M. P., and Viens, F. G.: Reconstructing past temperatures from natural proxies and estimated climate forcings using short- and long-memory models, Ann. Appl. Stat., 8, 1966–2001, 2014.

Büntgen, U., Allen, K., Anchukaitis, K. J., Arseneault, D., Boucher, É., Bräuning, A., Chatterjee, S., Cherubini, P., Churakova, O. V., Corona, C., Gennaretti, F., Grießinger, J., Guillet, S., Guiot, J., Gunnarson, B., Helama, S., Hochreuther, P., Hughes, M. K., Huybers, P., Kirdyanov, A. V., Krusic, P. J., Ludescher, J., Meier, W. J.-H., Myglan, V. S., Nicolussi, K., Oppenheimer, C., Reinig, F., Salzer, M. W., Seftigen, K., Stine, A. R., Stoffel, M., St. George, S., Tejedor, E., Trevino, A., Trouet, V., Wang, J., Wilson, R., Yang, B., Xu, G., and Esper, J.: The influence of decision-making in tree ring-based climate reconstructions, Nat. Commun., 12, 1–10, 2021.

Christiansen, B., Schmith, T., and Thejll, P.: A surrogate ensemble study of climate reconstruction methods: Stochasticity and robustness, J. Climate, 22, 951–976, https://doi.org/10.1175/2008JCLI2301.1, 2009.

Clement, A., Bellomo, K., Murphy, L. N., Cane, M. A., Mauritsen, T., Rädel, G., and Stevens, B.: The Atlantic Multidecadal Oscillation without a role for ocean circulation, Science, 350, 320–324, https://doi.org/10.1126/science.aab3980, 2015.

Duvenaud, D., Lloyd, J., Grosse, R., Tenenbaum, J., and Zoubin, G.: Structure discovery in nonparametric regression through compositional kernel search, in: International Conference on Machine Learning, edited by: Dasgupta, S. and McAllester, D., vol. 28, Proceedings of Machine Learning Research, PMLR, Atlanta, Georgia, USA, 1166–1174, https://proceedings.mlr.press/v28/duvenaud13.html (last access: 22 February 2024), 2013.

Esper, J., Frank, D. C., Wilson, R. J., and Briffa, K. R.: Effect of scaling and regression on reconstructed temperature amplitude for the past millennium, Geophys. Res. Lett., 32, L07711, https://doi.org/10.1029/2004GL021236, 2005.

Garuba, O. A., Lu, J., Singh, H. A., Liu, F., and Rasch, P.: On the relative roles of the atmosphere and ocean in the Atlantic multidecadal variability, Geophys. Res. Lett., 45, 9186–9196, https://doi.org/10.1029/2018GL078882, 2018.

Gent, P. R., Danabasoglu, G., Donner, L. J., Holland, M. M., Hunke, E. C., Jayne, S. R., Lawrence, D. M., Neale, R. B., Rasch, P. J., Vertenstein, M., Worley, P. H., Yang, Z.-L., and Zhang, M.: The community climate system model version 4, J. Climate, 24, 4973–4991, https://doi.org/10.1175/2011JCLI4083.1, 2011.

Giorgetta, M. A., Jungclaus, J., Reick, C., Legutke, S., Bader, J., Böttinger, M., Brovkin, V., Crueger, T., Esch, M., Fieg, K., Glushak, K., Gayler, V., Haak, H., Hollweg, H.-D., Ilyina, T., Kinne, S., Kornblueh, L., Matei, D., Mauritsen, T., Mikolajewicz, U., Mueller, W., Notz, D., Pithan, F., Raddatz, T., Rast, S., Redler, R., Roeckner, E., Schmidt, H., Schnur, R., Segschneider, J., Six, K., Stockhause, M., Timmreck, C., Wegner, J., Widmann, H., Wieners, K., Claussen, M., Marotzke, J., and Stevens, B.: Climate and carbon cycle changes from 1850 to 2100 in MPI-ESM simulations for the Coupled Model Intercomparison Project phase 5, J. Adv. Model. Earth Sy., 5, 572–597, https://doi.org/10.1002/jame.20038, 2013.

Gray, S. T., Graumlich, L. J., Betancourt, J. L., and Pederson, G. T.: A tree-ring based reconstruction of the Atlantic Multidecadal Oscillation since 1567 AD, Geophys. Res. Lett., 31, L12205, https://doi.org/10.1029/2004GL019932, 2004.

Hanhijärvi, S., Tingley, M. P., and Korhola, A.: Pairwise comparisons to reconstruct mean temperature in the Arctic Atlantic Region over the last 2,000 years, Clim. Dynam., 41, 2039–2060, https://doi.org/10.1007/s00382-013-1701-4, 2013.

Haustein, K., Otto, F. E., Venema, V., Jacobs, P., Cowtan, K., Hausfather, Z., Way, R. G., White, B., Subramanian, A., and Schurer, A. P.: A limited role for unforced internal variability in twentieth-century warming, J. Climate, 32, 4893–4917, https://doi.org/10.1175/JCLI-D-18-0555.1, 2019.

Hensman, J., Fusi, N., and Lawrence, N. D.: Gaussian processes for Big data, in: Proceedings of the Twenty-Ninth Conference on Uncertainty in Artificial Intelligence, ArXiv [preprint], https://doi.org/10.48550/arXiv.1309.6835, 2013.

Hunter, J. D.: Matplotlib: A 2D graphics environment, Comput. Sci. Eng., 9, 90–95, https://doi.org/10.1109/MCSE.2007.55, 2007.

Jones, P. D. and Mann, M. E.: Climate over past millennia, Rev. Geophys., 42, RG2002, https://doi.org/10.1029/2003RG000143, 2004.

Kilbourne, H., Yu, Z., Neukom, R., Nash, D., Gergis, J., Steig, E. J., Ge, Q., McKay, N. P., Kaufman, D. S., Curran, M. A. J., Thomas, E. R., Sigl, M., Thirumalai, K., Emile-Geay, J., Chen, M.-T., Seidenkrantz, M.-S., Turney, C., Jacques, J. S., Linderholm, H. W., Horiuchi, K., Björklund, J., Severi, M., Cook, E., Bertler, N., Isaksson, E., wahl, eugene, Leduc, G., Martrat, B., E Tierney, J., Goosse, H., Thamban, M., DeLong, K., Anchukaitis, K., Zinke, J., Uemura, R., Abram, N. J., Shao, X., Dixon, D., von Gunten, L., Wang, J., Addison, J., Evans, M. N., Henley, B., Zhixin, H., McGregor, H. V., Pederson, G. T., Stenni, B., Werner, J., Xu, C., Divine, D., Dixon, B. C., Mundo, I. A., Nakatsuka, T., Phipps, S. J., Routson, C., Tyler, J. J., Allen, K. J., Chase, B., de Jong, R., Ekaykin, A. A., Ersek, V., Filipsson, H. L., Francus, P., Freund, M., Frezzotti, M., Gaire, N., Gajewski, K., Gornostaeva, A., Grosjean, M., Hormes, A., Husum, K., Selvaraj, K., Kawamura, K., Nalan, K., Lorrey, A., Mikhalenko, V., Mortyn, G. P., Motoyama, H., Moy, A., Mulvaney, R., Munz, P., Oerter, H., Opel, T., Orsi, A., Ovchinnikov, D., Porter, T., Roop, H., Saenger, C., Sano, M., Sauchyn, D., Saunders, K., Sicre, M.-A., Sinclair, K., St George, S., Thapa, U., Viau, A., Vladimirova, D., and White, J.: A global multiproxy database for temperature reconstructions of the Common Era, figshare [data set], https://doi.org/10.6084/m9.figshare.c.3285353.v2, 2017.

Kingma, D. P. and Ba, J.: Adam: A method for stochastic optimization, arXiv [preprint], https://doi.org/10.48550/arXiv.1412.6980, 2014.

Knudsen, M. F., Jacobsen, B. H., Seidenkrantz, M.-S., and Olsen, J.: Evidence for external forcing of the Atlantic Multidecadal Oscillation since termination of the Little Ice Age, Nat. Commun., 5, 1–8, https://doi.org/10.1038/ncomms4323, 2014.

Kopp, R. E., Kemp, A. C., Bittermann, K., Horton, B. P., Donnelly, J. P., Gehrels, W. R., Hay, C. C., Mitrovica, J. X., Morrow, E. D., and Rahmstorf, S.: Temperature-driven global sea-level variability in the Common Era, P. Natl. Acad. Sci. USA, 113, E1434–E1441, https://doi.org/10.1073/pnas.1517056113, 2016.

Landrum, L., Otto-Bliesner, B. L., Wahl, E. R., Conley, A., Lawrence, P. J., Rosenbloom, N., and Teng, H.: Last millennium climate and its variability in CCSM4, J. Climate, 26, 1085–1111, https://doi.org/10.1175/JCLI-D-11-00326.1, 2013.

Mann, M. E., Zhang, Z., Hughes, M. K., Bradley, R. S., Miller, S. K., Rutherford, S., and Ni, F.: Proxy-based reconstructions of hemispheric and global surface temperature variations over the past two millennia, P. Natl. Acad. Sci. USA, 105, 13252–13257, https://doi.org/10.1073/pnas.0805721105, 2008.

Mann, M. E., Steinman, B. A., Brouillette, D. J., and Miller, S. K.: Multidecadal climate oscillations during the past millennium driven by volcanic forcing, Science, 371, 1014–1019, https://doi.org/10.1126/science.abc5810, 2021.

Mann, M. E., Steinman, B. A., Brouillette, D. J., Fernandez, A., and Miller, S. K.: On The Estimation of Internal Climate Variability During the Preindustrial Past Millennium, Geophys. Res. Lett., 49, e2021GL096596, https://doi.org/10.1029/2021GL096596, 2022.

Mansfield, L. A., Nowack, P. J., Kasoar, M., Everitt, R. G., Collins, W. J., and Voulgarakis, A.: Predicting global patterns of long-term climate change from short-term simulations using machine learning, npj Clim. Atmos. Sci., 3, 1–9, https://doi.org/10.1038/s41612-020-00148-5, 2020.

Matthews, A. G. d. G., Van Der Wilk, M., Nickson, T., Fujii, K., Boukouvalas, A., León-Villagrá, P., Ghahramani, Z., and Hensman, J.: GPflow: A Gaussian Process Library using TensorFlow, J. Mach. Learn. Res., 18, 1–6, 2017.

Mead, A.: Review of the Development of Multidimensional Scaling Methods, J. Roy. Stat. Soc. Ser. D, 41, 27–39, https://doi.org/10.2307/2348634, 1992.

Meehl, J.: CCSM4 coupled run for CMIP5 historical (1850–2005), World Data Center for Climate (WDCC) at DKRZ [data set], https://doi.org/10.1594/WDCC/CMIP5.NRS4hi, 2014.

Mette, M. J., Wanamaker Jr, A. D., Retelle, M. J., Carroll, M. L., Andersson, C., and Ambrose Jr., W. G.: Persistent multidecadal variability since the 15th century in the southern Barents Sea derived from annually resolved shell-based records, J. Geophys. Res.-Oceans, 126, e2020JC017074, https://doi.org/10.1029/2020JC017074, 2021.

Michel, S., Swingedouw, D., Chavent, M., Ortega, P., Mignot, J., and Khodri, M.: Reconstructing climatic modes of variability from proxy records using ClimIndRec version 1.0, Geosci. Model Dev., 13, 841–858, https://doi.org/10.5194/gmd-13-841-2020, 2020.

Miles, M. W., Divine, D. V., Furevik, T., Jansen, E., Moros, M., and Ogilvie, A. E.: A signal of persistent Atlantic multidecadal variability in Arctic sea ice, Geophys. Res. Lett., 41, 463–469, https://doi.org/10.1002/2013GL058084, 2014.

Otto-Bliesner, B.: CCSM4 coupled simulation for CMIP5 past 1000 years (850–1850) with natural forcings, World Data Center for Climate (WDCC) at DKRZ [data set], https://doi.org/10.1594/WDCC/CMIP5.NRS4pk, 2014.

PAGES2k: A global multiproxy database for temperature reconstructions of the Common Era, Sci. Data, 4, 170088, https://doi.org/10.1038/sdata.2017.88, 2017.

PAGES2k: Consistent multi-decadal variability in global temperature reconstructions and simulations over the Common Era, Nat. Geosci., 12, 643, https://doi.org/10.1038/s41561-019-0400-0, 2019.

Pedregosa, F., Varoquaux, G., Gramfort, A., Michel, V., Thirion, B., Grisel, O., Blondel, M., Prettenhofer, P., Weiss, R., Dubourg, V., Vanderplas, J., Passos, A., Cournapeau, D., Brucher, M., Perrot, M., and Duchesnay, E.: Scikit-learn: Machine learning in Python, J. Mach. Learn. Res., 12, 2825–2830, 2011.

Rasmussen, C. E. and Williams, C. K. I.: Gaussian processes for machine learning, vol. 2, MIT press Cambridge, MA, https://doi.org/10.7551/mitpress/3206.001.0001, 2006.

Saenger, C., Cohen, A. L., Oppo, D. W., Halley, R. B., and Carilli, J. E.: Surface-temperature trends and variability in the low-latitude North Atlantic since 1552, Nat. Geosci., 2, 492–495, https://doi.org/10.1038/ngeo552, 2009.

Särkkä, S.: Bayesian filtering and smoothing, 3, Cambridge University Press, https://doi.org/10.1017/CBO9781139344203, 2013.

Singh, H. K. A., Hakim, G. J., Tardif, R., Emile-Geay, J., and Noone, D. C.: Insights into Atlantic multidecadal variability using the Last Millennium Reanalysis framework, Clim. Past, 14, 157–174, https://doi.org/10.5194/cp-14-157-2018, 2018.

Smerdon, J. E.: Climate models as a test bed for climate reconstruction methods: pseudoproxy experiments, Wires Clim. Change, 3, 63–77, https://doi.org/10.1002/wcc.149, 2012.

Smerdon, J. E., Kaplan, A., Zorita, E., González-Rouco, J. F., and Evans, M.: Spatial performance of four climate field reconstruction methods targeting the Common Era, Geophys. Res. Lett., 38, L11705, https://doi.org/10.1029/2011GL047372, 2011.

Svendsen, L., Hetzinger, S., Keenlyside, N., and Gao, Y.: Marine-based multiproxy reconstruction of Atlantic multidecadal variability, Geophys. Res. Lett., 41, 1295–1300, https://doi.org/10.1002/2013GL059076, 2014.

Von Storch, H., Zorita, E., Jones, J. M., Dimitriev, Y., González-Rouco, F., and Tett, S. F.: Reconstructing past climate from noisy data, Science, 306, 679–682, https://doi.org/10.1126/science.1096109, 2004.

von Storch, H., Zorita, E., and González-Rouco, F.: Assessment of three temperature reconstruction methods in the virtual reality of a climate simulation, Int. J. Earth Sci., 98, 67–82, https://doi.org/10.1007/s00531-008-0349-5, 2009.

Wang, J., Yang, B., Ljungqvist, F. C., Luterbacher, J., Osborn, T. J., Briffa, K. R., and Zorita, E.: Internal and external forcing of multidecadal Atlantic climate variability over the past 1,200 years, Nat. Geosci., 10, 512–517, https://doi.org/10.1038/ngeo2962, 2017.

Wegmann, M. and Jaume-Santero, F.: Artificial intelligence achieves easy-to-adapt nonlinear global temperature reconstructions using minimal local data, Commun. Earth Environ., 4, 217, https://doi.org/10.1038/s43247-023-00872-9, 2023.

Yan, X., Zhang, R., and Knutson, T. R.: A multivariate AMV index and associated discrepancies between observed and CMIP5 externally forced AMV, Geophys. Res. Lett., 46, 4421–4431, https://doi.org/10.1029/2019GL082787, 2019.

Zhang, R. and Delworth, T. L.: Impact of Atlantic multidecadal oscillations on India/Sahel rainfall and Atlantic hurricanes, Geophys. Res. Lett., 33, L17712, https://doi.org/10.1029/2006GL026267, 2006.

Zhang, R., Delworth, T. L., and Held, I. M.: Can the Atlantic Ocean drive the observed multidecadal variability in Northern Hemisphere mean temperature?, Geophys. Res. Lett., 34, L02709, https://doi.org/10.1029/2006GL028683, 2007.

Zhang, R., Sutton, R., Danabasoglu, G., Kwon, Y.-O., Marsh, R., Yeager, S. G., Amrhein, D. E., and Little, C. M.: A review of the role of the Atlantic meridional overturning circulation in Atlantic multidecadal variability and associated climate impacts, Rev. Geophys., 57, 316–375, https://doi.org/10.1029/2019RG000644, 2019.

Zhang, Z., Wagner, S., Klockmann, M., and Zorita, E.: Evaluation of statistical climate reconstruction methods based on pseudo-proxy experiments using linear and machine-learning methods, Clim. Past, 18, 2643–2668, https://doi.org/10.5194/cp-18-2643-2022, 2022.

Zorita, E., González-Rouco, F., and Legutke, S.: Testing the approach to paleoclimate reconstructions in the context of a 1000-yr control simulation with the ECHO-G coupled climate model, J. Climate, 16, 1378–1390, https://doi.org/10.1175/1520-0442(2003)16<1378:TTMEAA>2.0.CO;2, 2003.